Theses and Dissertations   1. Thesis and Dissertation Collection, all items

2020-06

FEASIBILITY OF UNDERWATER MEMS DF ACOUSTIC SENSOR FOR NARROWBAND DETECTION

Roberts, Jason

Monterey, California. Naval Postgraduate School

https://hdl.handle.net/10945/72091

NAVAL
POSTGRADUATE
SCHOOL

MONTEREY, CALIFORNIA

THESIS

**FEASIBILITY OF UNDERWATER MEMS DF
ACOUSTIC SENSOR FOR NARROWBAND DETECTION**

by

Jason Roberts

June 2020

Thesis Advisor:	Gamani Karunasiri
Co-Advisor:	Fabio D. Durante Pereira Alves

Approved for public release. Distribution is unlimited.

THIS PAGE INTENTIONALLY LEFT BLANK

REPORT DOCUMENTATION PAGE		*Form Approved OMB No. 0704-0188*

Public reporting burden for this collection of information is estimated to average 1 hour per response, including the time for reviewing instruction, searching existing data sources, gathering and maintaining the data needed, and completing and reviewing the collection of information. Send comments regarding this burden estimate or any other aspect of this collection of information, including suggestions for reducing this burden, to Washington headquarters Services, Directorate for Information Operations and Reports, 1215 Jefferson Davis Highway, Suite 1204, Arlington, VA 22202-4302, and to the Office of Management and Budget, Paperwork Reduction Project (0704-0188) Washington, DC 20503.

1. AGENCY USE ONLY *(Leave blank)*	2. REPORT DATE June 2020	3. REPORT TYPE AND DATES COVERED Master's thesis
4. TITLE AND SUBTITLE FEASIBILITY OF UNDERWATER MEMS DF ACOUSTIC SENSOR FOR NARROWBAND DETECTION		5. FUNDING NUMBERS RPN08; RPNVM
6. AUTHOR(S) Jason Roberts		
7. PERFORMING ORGANIZATION NAME(S) AND ADDRESS(ES) Naval Postgraduate School Monterey, CA 93943-5000		8. PERFORMING ORGANIZATION REPORT NUMBER
9. SPONSORING / MONITORING AGENCY NAME(S) AND ADDRESS(ES) Space & Naval Warfare Systems Center-Pacific , San Diego, CA 92110; Office of Naval Research, Arlington, VA 22203		10. SPONSORING / MONITORING AGENCY REPORT NUMBER
11. SUPPLEMENTARY NOTES The views expressed in this thesis are those of the author and do not reflect the official policy or position of the Department of Defense or the U.S. Government.		
12a. DISTRIBUTION / AVAILABILITY STATEMENT Approved for public release. Distribution is unlimited.		12b. DISTRIBUTION CODE A

13. ABSTRACT (maximum 200 words)

A microelectromechanical system (MEMS)–based directional sound sensor has been developed to operate both in air and underwater. The sensor consists of two wings that are attached to a substrate using two torsional legs at the middle as detailed in several previous theses. Though it was highly successful in operating in the air application, its underwater operation required it to be immersed in a liquid with impedance matching housing. The fluid strongly alters the operating characteristics of the sensor and reduces the sensitivity due to added viscous damping. In this thesis, two new MEMS sensors, designed to operate at 300 Hz and 520 Hz, were characterized both in air and underwater. For the measurements, the MEMS sensors were first integrated with newly designed readout electronics, which were needed to overcome the problems encountered with the off-the-shelf electronics employed in earlier studies. The new electronics were found to be highly stable and operated well when immersed in silicone oil used for underwater packaging of the sensors. The measured frequency responses were found to match with that of the simulations carried out using COMSOL finite element modeling. In addition, the sensors also show expected cosine directional characteristics. The research findings show that the MEMS-based sensors can be successfully operated in an underwater environment for determining the bearing of sound sources.

14. SUBJECT TERMS MEMS, acoustics, acoustic detectors, underwater, microphone, narrowband detection			15. NUMBER OF PAGES 85
			16. PRICE CODE
17. SECURITY CLASSIFICATION OF REPORT Unclassified	18. SECURITY CLASSIFICATION OF THIS PAGE Unclassified	19. SECURITY CLASSIFICATION OF ABSTRACT Unclassified	20. LIMITATION OF ABSTRACT UU

THIS PAGE INTENTIONALLY LEFT BLANK

FEASIBILITY OF UNDERWATER MEMS DF ACOUSTIC SENSOR FOR NARROWBAND DETECTION

Jason Roberts
Lieutenant, United States Navy
BSAE, University of Florida, 2012
BSME, University of Florida, 2012

Submitted in partial fulfillment of the
requirements for the degree of

MASTER OF SCIENCE IN APPLIED PHYSICS

from the

**NAVAL POSTGRADUATE SCHOOL
June 2020**

Approved by: Gamani Karunasiri
                Advisor

                Fabio D. Durante Pereira Alves
                Co-Advisor

                Kevin B. Smith
                Chair, Department of Physics

THIS PAGE INTENTIONALLY LEFT BLANK

ABSTRACT

A microelectromechanical system (MEMS)–based directional sound sensor has been developed to operate both in air and underwater. The sensor consists of two wings that are attached to a substrate using two torsional legs at the middle as detailed in several previous theses. Though it was highly successful in operating in the air application, its underwater operation required it to be immersed in a liquid with impedance matching housing. The fluid strongly alters the operating characteristics of the sensor and reduces the sensitivity due to added viscous damping. In this thesis, two new MEMS sensors, designed to operate at 300 Hz and 520 Hz, were characterized both in air and underwater. For the measurements, the MEMS sensors were first integrated with newly designed readout electronics, which were needed to overcome the problems encountered with the off-the-shelf electronics employed in earlier studies. The new electronics were found to be highly stable and operated well when immersed in silicone oil used for underwater packaging of the sensors. The measured frequency responses were found to match with that of the simulations carried out using COMSOL finite element modeling. In addition, the sensors also show expected cosine directional characteristics. The research findings show that the MEMS-based sensors can be successfully operated in an underwater environment for determining the bearing of sound sources.

THIS PAGE INTENTIONALLY LEFT BLANK

TABLE OF CONTENTS

LIST OF FIGURES

THIS PAGE INTENTIONALLY LEFT BLANK

LIST OF TABLES

THIS PAGE INTENTIONALLY LEFT BLANK

LIST OF ACRONYMS AND ABBREVIATIONS

DC   Direct Current

FWHM   Full Width Half Maximum

MEMS   Microelectromechanical System

NOA68   Norland Optical Adhesive 68

NPS   Naval Postgraduate School

SNR   Signal-to-Noise Ratio

SOI   Silicon-on-Insulator

SPL   Sound Pressure Level

TA   Towed Array

THIS PAGE INTENTIONALLY LEFT BLANK

ACKNOWLEDGMENTS

First, I would like to thank Dr. Gamani Karunasiri and Dr. Fabio Alves. Dr. Karunasiri's vision for this project far exceeded my own, and I am honored to have been a part of it. Dr. Alves is a fantastic mentor and was critical in helping me organize my thoughts and help me find my direction when I was lost. His wizardry in electronics saved me more than once when I thought something in my experimental setup was broken.

I would also like to thank Dr. Renato Rabello and Brian Gureck. If Dr. Karunasiri is the brains of the project, then Dr. Rabello is the spine and spinal cord. His work in fabricating and characterizing the sensor electronics was astounding, and my research would have been insignificant if it were not for him. Brian, my comrade in physics, helped make the daunting task of a thesis more enjoyable and was always available to point out the things I had managed to overlook.

Thank you to Steve Jacobs, who helped in fabricating the parts to make this research happen. Thank you to Jaehyun Park and Alberto Espinosa, whose prior research provided the background for my continuation on this project.

This work also would not have been possible without the gracious funding from the Office of Naval Research and the Space & Naval Warfare Systems Center-Pacific. The continued support from both organizations has been critical to keeping the U.S. Navy and the United States on the forefront of technological innovation. I am grateful to have been able to contribute to that innovation through their support.

Finally, I would like to thank my wife, Amanda, who convinced me to come to the Naval Postgraduate School in the first place. She knew what I wanted to do in my life when I still couldn't see past the end of the week. Her selflessness and compassion did more to help me grow and learn than she will ever realize. I love you and we did it.

THIS PAGE INTENTIONALLY LEFT BLANK

I. INTRODUCTION

Detection of sound sources has been the primary method of identifying and combating submarines since the introduction of the first German U-boat in World War I. The two detection methods, passive and active, operate on the same physical principle; a source generates sound, which propagates through a medium, until it reaches a detector. Most detection is done passively, because active detection requires the tracking submarine to reveal its presence to the target. Submarines have also become increasingly quieter. Improvements in sound dampening materials on submarine hulls and machinery, longer running batteries, and improved hull design all contribute to reducing the acoustic profile of a target. As noise cancellation technology improves, innovations in passive sound detection are necessary to maintain the competitive edge for tracking underwater contacts. One innovation is an underwater sensor derived from the auditory functions of the *Ormia ochracea* fly, in development at the Naval Postgraduate School (NPS).

A. BACKGROUND

1. Current Underwater Sound Detection Technology

Typical underwater sound sensors, or hydrophones, are omnidirectional microphones that can be assembled into an array to determine the bearing of sound [1]. The array generates signal due to time-dependent pressure changes that can be analyzed to determine the bearing. Directionality of the sound source is determined by the physical spacing of the hydrophones and at what time a pressure wave reaches each of the individual hydrophones. The most common form of sonar array used onboard surface ships and submarines is the towed array (TA). Additional array types, such as the spherical array, bow array, and flank array are employed on submarines around the world; however, only the towed array will be discussed here. Towed arrays are comprised of linearly spaced hydrophones along a cable as illustrated in Figure 1.
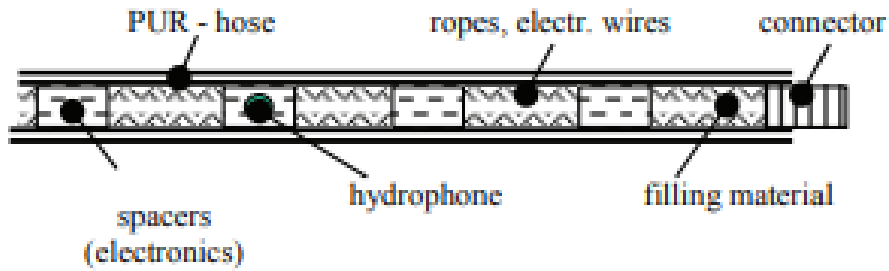
Figure 1.   Sectional diagram of a TA. Source: [2].

The length of the towed array is dependent on the strength of the materials comprising the towed array cable. The hydrophone spacing is determined by wavelength of the incident sound. In addition to the sensing portion of the cable, an additional length of wire containing cable is attached to distance the hydrophones from the towing vessel, usually multiple kilometers away [3]. This reduces the background noise levels at the hydrophones and improves the Signal-to-Noise Ratio (SNR) of the TA [2]. Advances such as fiber optics have allowed the number of hydrophones in an array to increase dramatically, without significantly impacting cable weight or cable width, which became prohibitive with copper wiring [4].

The human hearing system can resolve directionality to a single location [5], while the TA can only resolve directionality to two possible locations. Because a TA is a linear array, the incident sound wave arrives along a conical bearing to the TA. Underwater, this results not only in the true bearing of the sound source, but also an additional ambiguous bearing as illustrated in Figure 2.
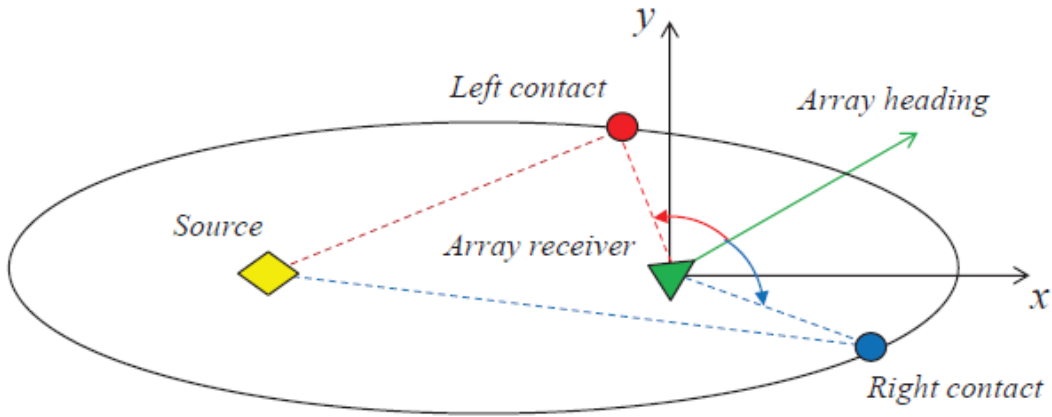
Due to receiving sound along a conical bearing, the TA interprets incident sound pressure as coming from two possible locations. The true bearing (in red) and the ambiguous bearing (in blue). The magnitude of the angle between the array heading (green) and each of the bearings is the same, only the direction is different.

Figure 2.   Diagram of how a TA receives sound. Adapted from [6].

Alternative direction sensing methods include the use of vector sensors, which are designed to acquire vector quantities associated with the sound field [7]–[12]. Commonly, these sensors operate via the measurement of a pressure gradient [9] or particle velocity due to motion of the medium [10]. The Hydroflown vector sensor measures particle velocity by measuring the temperature difference between two parallel platinum hot-wire resistors [12]. The Wilcoxon vector sensor uses three lead magnesium niobate-lead titanate (PMN-PT) crystal-based axial accelerometers and a lead zirconate titanate (PZT) omnidirectional hydrophone to determine directionality [13]. The measurement of particle velocity using neutrally buoyant objects that are displaced by the incident acoustic pressure wave has also been explored [14].

2.   MEMS Sensor Based on the *Ormia Ochracea*

The *Ormia ochracea* is a parasitic fly that lays its eggs on a cricket. The fly has eardrums that are approximately 0.5 mm apart and the cricket emits a chirp of 4.8 kHz [5]. The chirp frequency corresponds to a wavelength of about 7 cm. Because the wavelength of the sound is about two orders of magnitude larger than the eardrum separation of the fly, the fly's eardrums cannot operate on the same physical principles as human hearing.

The *Ormia ochracea* has evolved a novel way of hearing the high frequency chirp of the host cricket. Instead of having separate eardrums, the fly's eardrums are connected by a cartilaginous bridge [5]. When in incident pressure wave acts on the eardrums, the bridge allows the transfer of some of the mechanical energy between them. This mechanical system allows the eardrums to oscillate in a bending mode at one frequency and a rocking mode at a different frequency. A photograph of the fly's eardrums along with the mechanical model of the eardrums are shown in Figure 3 [5].
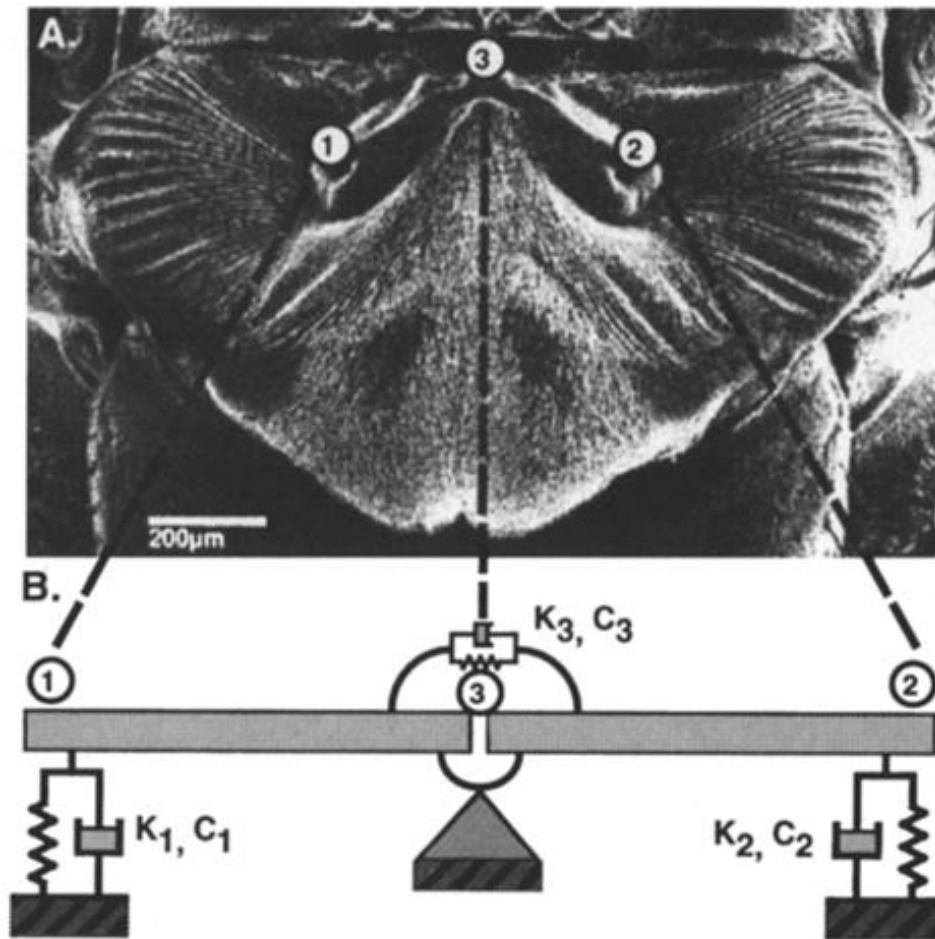
Figure 3.   Eardrums of the *Ormia ochracea* and the mechanical model.
Source: [5].

The bending mode of the fly's eardrums is excited by the overall sound pressure level (SPL) of the incident sound, while the rocking mode is excited by the pressure

difference between the eardrums [5]. The superposition of these two modes allows the fly to accurately localize sound sources having wavelengths multiple orders of magnitude longer than the separation distance between the fly's eardrums [5].

3. NPS Developed MEMS Sensor in an Underwater Environment

A Microelectromechanical system (MEMS) based directional sound sensor has been in development at the NPS Sensor Research Lab since 2006. Swan [15] created the first MEMS sensor design for an underwater application. The sensor needed to be housed in an acoustically permeable container for the desired sound frequency and the housing needed to be filled with a medium that had an acoustical impedance close to that of water [16]. The medium also needed to be electrically insulating to allow the sensor readout electronics to operate. In addition, the medium needed to have low viscosity to minimize fluid damping on the moving structures of the sensor. Figure 4 shows the first generation of the MEMS sensor developed at the NPS Sensor Research Lab for underwater operation.
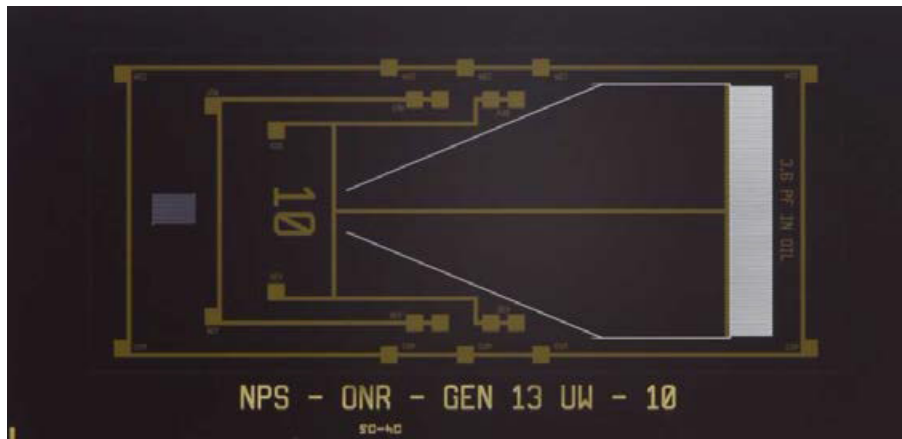
Figure 4.   First generation of the underwater MEMS sensor. Source: [16].

Multiple iterations of the sensor housing have been created since the first design in 2016. Originally, the MEMS sensor housing used a boot comprised of Flexane-80, which has a speed of sound of 2400 ± 25 m/sec and a density of 1045 kg/m^3. Da Re [16] found that the Flexane-80 attenuated sound transmission in some regions of the frequency spectrum between 50 and 600 Hz, while enchasing sound transmission in other regions of

5

the spectrum. Figure 5 shows the measured sound signal using a hydrophone with and without the housing (boot) attached to it [16].
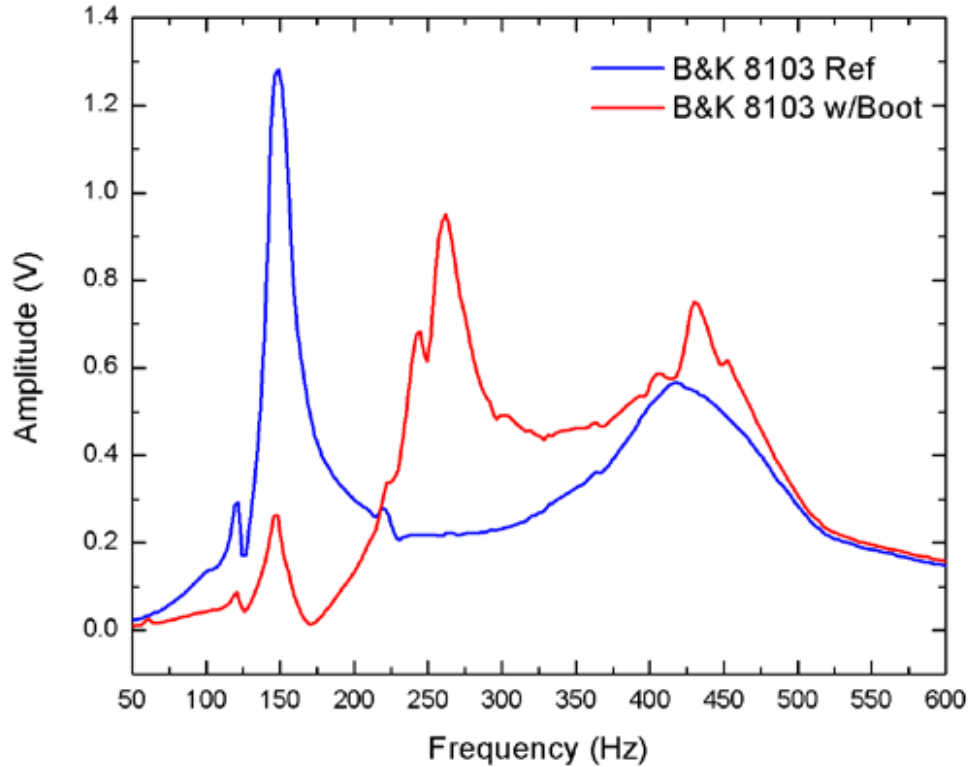
Comparison between the reference hydrophone with and without enclosure. The presence of the boot reduces the response in the low frequency range (50-200 Hz) while gaining between 225–400 Hz. This effect is minimal above 400 Hz.

Figure 5.   The effect of Flexane-80 boot on transmission between 50 and 600 Hz. Source: [16].

Da Re [16] recommended replacing the Flexane-80 with another castable material, whose properties would allow for unity or near unity transmission through the boot in the tested frequency range. Subsequent research showed that PMC-780 yielded near unity transmission over the frequency range from 50 to 600 Hz [17] as shown in Figure 6. Additionally, multiple boot thicknesses were also tested by Espinoza [17]. It was found that for PMC-780, the transmission through the boot was independent of the thickness of the boot wall, allowing for robust sensor packaging without impacting sensor performance.
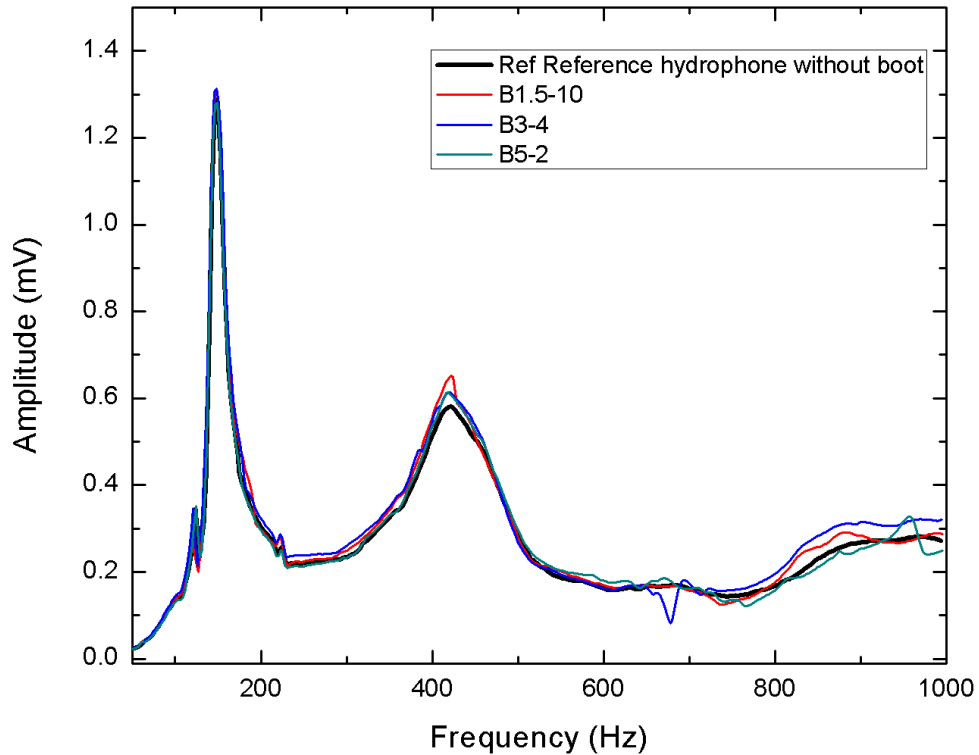
Comparison of signals from the B&K 8103 reference hydrophone submerged in water (black) and the reference hydrophone encased in the sensor housing with a PMC-780 boot thickness of 1.5 mm (red), 3.0 mm (blue), and 5.0 mm (teal).

Figure 6.   Sensitivity comparison for PMC-780. Adapted from [17].

The original housing design also used PSF-2cSt silicone oil as an insulative medium in which the sensor could be submerged [15]. This silicone oil was chosen due to its low viscosity (2 cSt) and because its density was close to that of pure water (873 kg/m^3) [18]. Subsequent housing iterations changed from PSF-2cSt to PSF-1cSt silicone oil to further reduce the damping though it resulted in a decrease in the density of the insulative fluid (818 kg/m^3) [19].

The sensor has also been updated since the first-generation design used by Swan. The new design uses two wings, with capacitive comb fingers on the outer edges, attached by a single bridge. The bridge is attached to the silicon substrate by two torsional legs. This allows the sensor to operate in both the bending modes and rocking modes. Due to the longer wavelengths associated with underwater sound, the sensor response at the rocking

mode frequency is orders of magnitude less than the response at the bending mode frequency.

B. OBJECTIVE AND THESIS ORGANIZATION

The objective of this thesis is broken into two parts. First, modifications to the *Ormia* based sensor will be explored using finite element modeling software to improve sensor response in subsequent experimental trials. Second, the effects of improvements to sensor housing, packaging, and electronic readout on the experimental sensor performance will be analyzed.

This thesis is organized into five parts. Chapter I presents a discussion on currently employed TA sensor technology, the *Ormia ochracea* basis for the sensor construction, and a brief evolution of the *Ormia* based sensor at the NPS Sensor Research Lab.

Chapter II discusses the parameters of the current generation of the MEMS direction-based sound sensor for air and underwater purposes. It also discusses the finite element model used in COMSOL as well as simulated performance of the current generation sensor and suggested optimization.

Chapter III covers the experimental setup for testing the *Ormia* based sensor in the anechoic chamber for air testing and the underwater anechoic chamber for underwater tests. This section also discusses development and design of the sensor housing and circuitry for both air and underwater testing.

Chapter IV discusses the results of testing the sensor both in air and underwater.

Chapter V presents research conclusions and recommendations for future work.

II.   SENSOR EVOLUTION AND MODELING

A.   CURRENT SENSOR DESIGN

Multiple changes have been made from the sensors used by Swan [15] and Da Re [16]. The current sensor generation (Gen 6), as shown in Figure 7, no longer consists of a single wing sensor, but two wings connected by a bridge to two torsional legs attached to the Silicon substrate. This design allows for detection of both the bending and rocking modes and more closely matches the *Ormia*'s hearing structure. Previous sensor generations attached the bridge to the inner edge of the wing. When the wing was etched to release from the substrate, the wing would flex vertically, due to the residual stresses in the Si substrate [20], [21]. This reduced the region of overlap between the wing and substrate comb finger pairs. Generation six attaches the bridge to approximately the middle of the wing. This reduces the warp of the sensor structure, increasing the overlap between the wing and substrate comb finger, resulting in a larger capacitance when the sensor is under no load. The sensor also no longer employs the trapezoidal wing configuration that was used by Swan [15]. Instead, the sensor has square wings that allows for better response control. Figure 7 shows a micrograph of a Gen 6 MEMS based direction finding acoustic sensor.
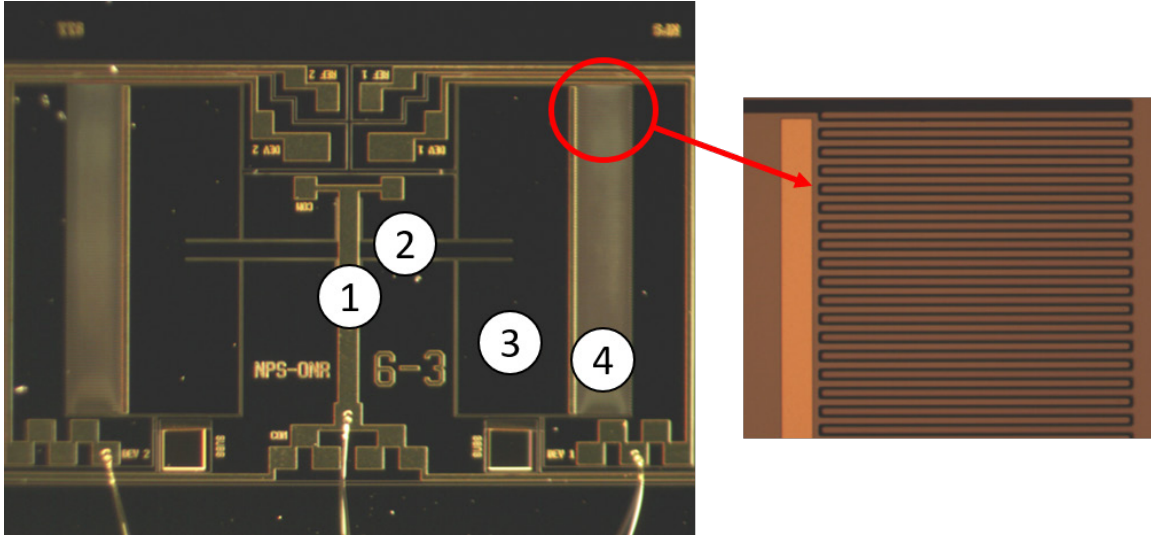
Sensor components: (1) leg, (2) bridge, (3) wing, (4) capacitive comb fingers.

Figure 7.   Gen 6-3 sensor designed at NPS (left). Zoomed in view of (4) (right).

The two sensors used for this research are generation 6-3 and 6-4. At the end of each wing is a set of interdigitated capacitive comb fingers that allow for a voltage readout when electrical power is supplied to the sensor. The sensors are fabricated using a 400 μm silicon-on-insulator (SOI) substrate with a device layer of 25 μm. The sensors are mounted in a recessed location in the readout circuit board that is approximately 1.0 mm thick. Table 1 shows a comparison between the sensor specific parameters of the 6-3 and 6-4 MEMS acoustic sensors. The two sensors are identical except the size of bridges and legs. Figure 8 shows corresponding dimensions on the 6-3 sensor.

Table 1.   Design parameters of the 6-3 and 6-4 MEMS acoustic
sensors. Units are μm.

Parameters	6-3 Sensor Dimension	6-4 Sensor Dimension
Bridge Length	3000	3000
Bridge Width	150	500
Leg Length	200	300
Leg Width	400	200
Wing Length	1095	1095
Wing Width	3000	3000
Comb Finger Length	500	500
Comb Finger Width	10	10
Comb Finger Channel Width	5	5
Sensor Channel Width	20	20
Overall Sensor Length	5400	5400
Overall Sensor Width	3040	3040
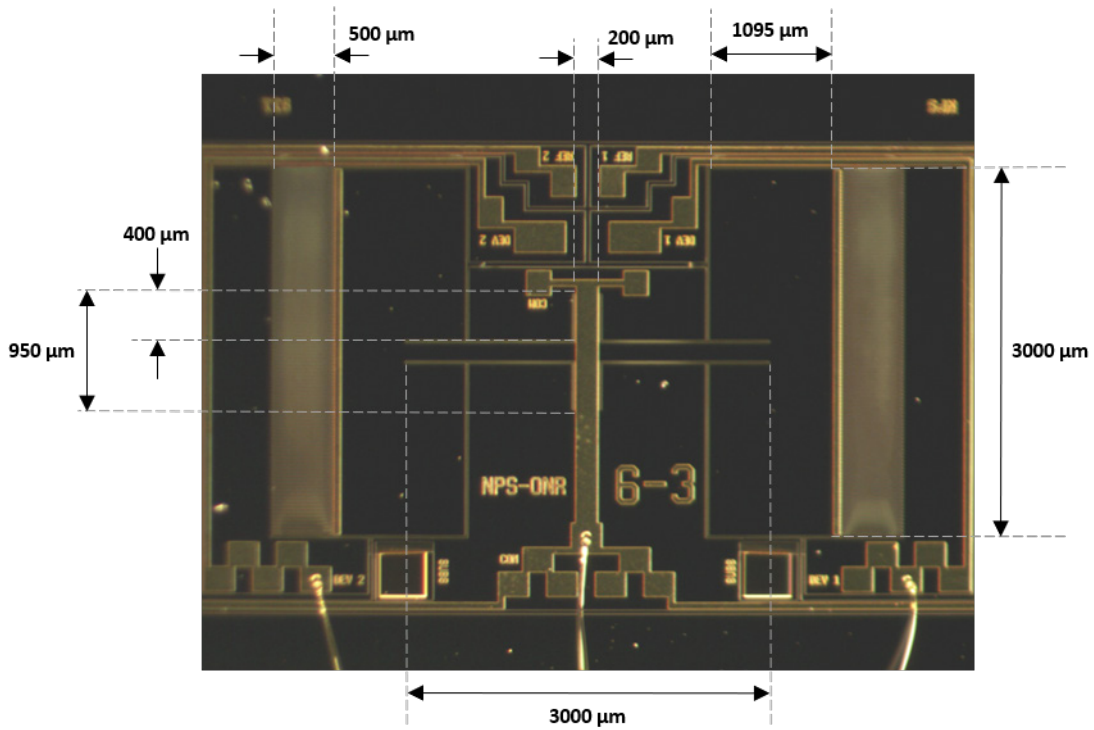
Figure 8.   Dimensions for the 6-3 sensor corresponding to Table 1.

B.   FINITE ELEMENT MODELING

Finite element modeling of both sensors was performed using COMSOL Multiphysics, version 5.4 [22]. The modeling for this research focuses only on the bending mode of oscillation for the MEMS sensors since it is difficult to observe the rocking mode underwater due to the long sound wavelengths involved and damping generated by the use of PSF-1cSt silicone oil for packaging the sensors. This allows the model to be cut in half along the torsional leg axis since the bending mode is symmetric with respect to the bridge axis. In addition, further reduction of the structure in the simulation can be done due to the symmetry of the sensor geometry along the bridge axis. The simulation model is a quartered version of the total structure with symmetry boundary conditions that can substantially reduce the simulation time. Figure 9 shows the 2D geometry of the simulated sensor. Figure 10 shows the 3D reduced geometry used for the simulation
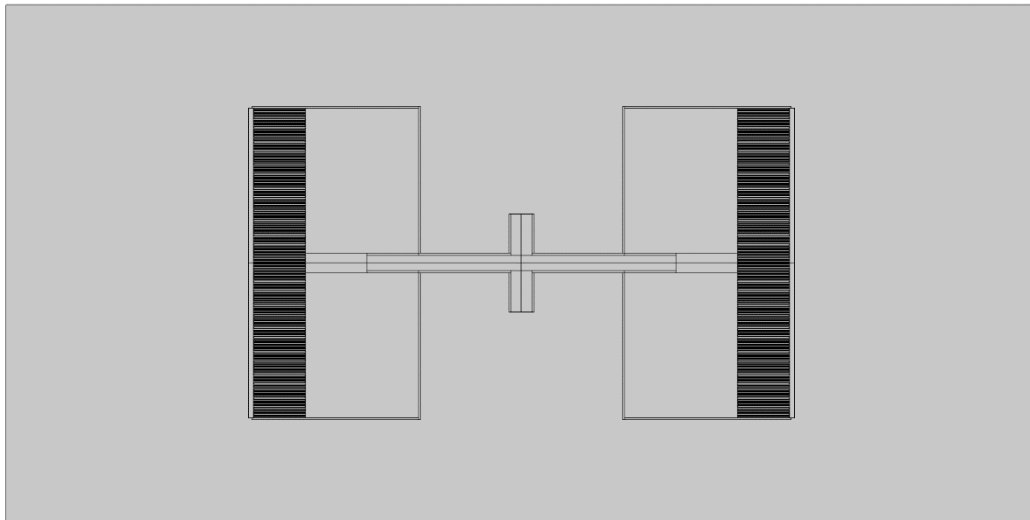
Figure 9.   Two-dimensional geometry of the Gen 6-3 sensor used in the COMSOL model.
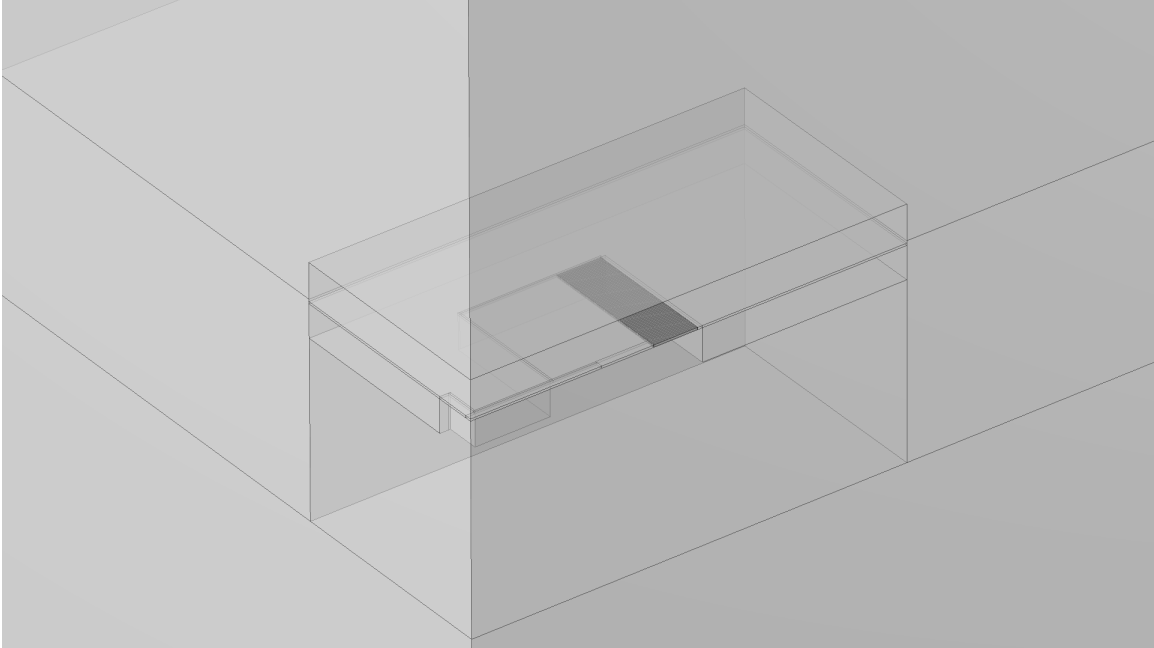
Figure 10.   Three-dimensional geometry of the 6-3 sensor and circuit board
used in COMSOL.

The simulation employs three sets of physics for modeling the MEMS sensor. The sensor is modeled using solid mechanics applied to anisotropic silicon (2330 kg/m^3) using a stress tensor [22]. In the far-field, pressure acoustics is employed. In the regions including and immediately surrounding the flexing wing of the sensor, thermoviscous acoustics is employed to correctly model the viscous fluid flow around the wings and in between the interdigitated comb fingers. In the region where the comb fingers fully overlap, Couette flow is expected. In the region where the comb fingers do not overlap at all, Hagen-Poiseuille flow is expected. Both types of flow occur in between full overlap and no overlap [23]. Figure 11 shows a fluid model diagram of the Couette and Hagen-Poiseuille flows. The thermoviscous physics employs Navier-Stokes equations as well as drag damping to take these into effect.
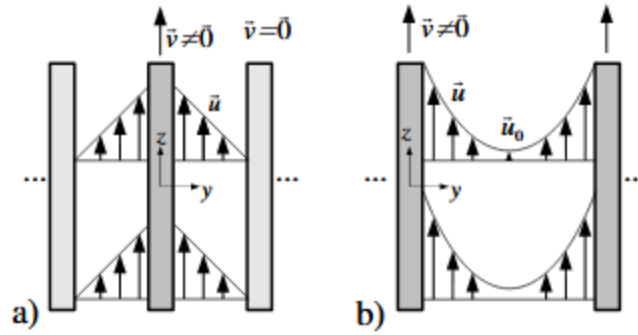
Figure 11.   Flow profiles experienced by the interdigitated comb fingers. a) Couette flow b) Hagen-Poiseuille flow. Source: [23].

C.   EXECUTED SIMULATIONS AND RESULTS

Four studies are conducted for each of the 6-3 and 6-4 sensors. First, the frequency response is determined for each sensor in air. Second, the directional response of each sensor is simulated. It is expected that at the bending mode, each sensor exhibits a dual lobe pattern, with displacement peaks when the sound source is either directly in front of or directly behind the sensor and valleys when the sound source is perpendicular to the face of the sensor. These two simulations are repeated with the sensor immersed in PSF-1cSt silicone oil instead of air. The final simulation is carried out using the 6-3 sensor and explores the optimum spacing between the comb fingers to maximize the displacement of the sensor when operated at its resonant frequency.

1.   Gen 6-3 Sensor Simulated in Air

The simulated frequency response of the 6-3 sensor is shown in Figure 12. The simulated frequency peak occurs at 1488 Hz with a displacement amplitude of 1.83 µm/Pa. The bandwidth at Full Width Half Maximum (FWHM) is about 66 Hz. Figure 13 shows the normalized simulated directional response of the 6-3 sensor. The simulation predicts a two-lobe pattern with response peaks at the 0° and 180° positions and troughs at the 90° and 270° positions as expected for a pressure gradient microphone [24].
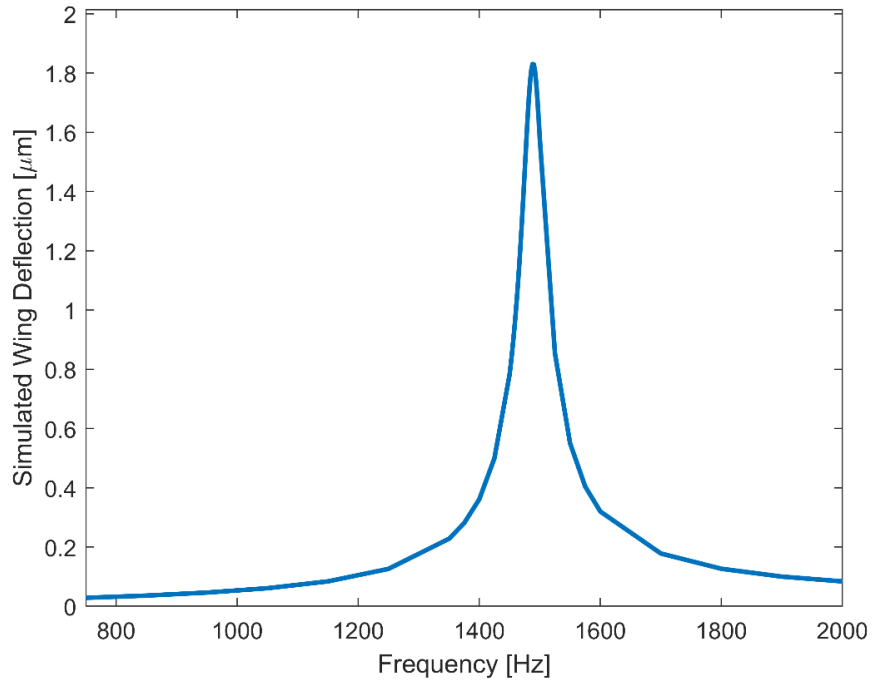
Figure 12.   Simulated frequency response of a Gen 6-3 sensor with bending resonance at 1488 Hz.

Figure 13.   Simulated normalized directional response of the 6-3 sensor in air at resonance (1488 Hz).

2. Gen 6-3 Sensor in Oil

Figure 14 shows the simulated frequency response of the 6-3 sensor when immersed in PSF-1cSt silicone oil. The maximum displacement of the sensor is about 24 nm/Pa. The simulated frequency peak occurs at 248 Hz, six times smaller than the simulated frequency peak in air. The shift of the peak position to a lower frequency is primarily due to mass loading by higher density (818 kg/m^3) silicone oil. The FWHM of the sensor at is found to be about 121 Hz, which is about a factor of two times larger than the simulated value in air of 66 Hz originated from higher viscous damping generated by silicone oil. Figure 15 shows the simulated normalized directional response of the 6-3 sensor when operated in oil. The two-lobe pattern remains when replacing the operating medium (air) with the silicone oil.

Figure 14.   Simulated frequency response of the 6-3 sensor in PSF-1cSt.
Resonance occurs at 248 Hz.
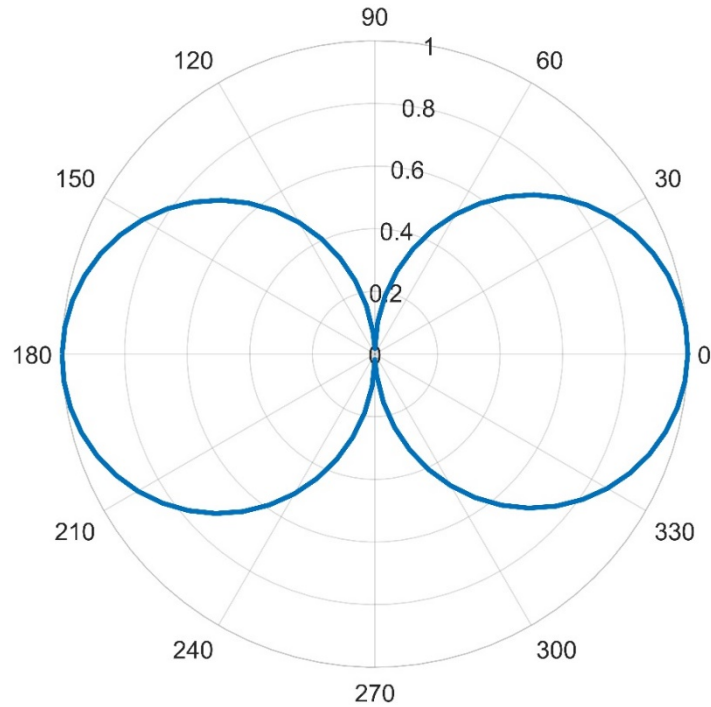
Figure 15.   Simulated normalized directional response of the 6-3 sensor in PSF-1cSt at resonance (248 Hz).

3.   Gen 6-4 Sensor in Air

The simulated frequency response of the 6-4 sensor is shown in Figure 16. The simulated frequency peak occurs at 2676 Hz with a displacement amplitude of about 22 µm/Pa. The higher bending resonance frequency is due to the thicker bridge used for the sensor. The FWHM is found to be about 77 Hz, which is close to that of the 6-3 sensor. Figure 17 shows the normalized simulated directional response of the 6-4 sensor. Similar to the 6-3 directional simulation, it shows a two-lobe pattern with response peaks at the 0° and 180° positions and troughs at the 90° and 270° positions.
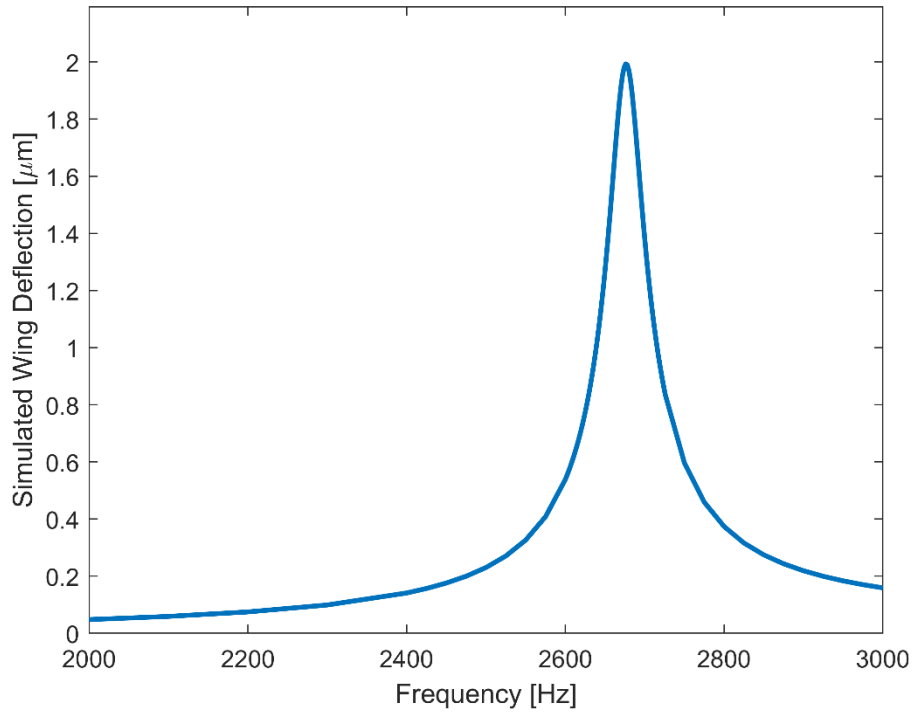
Figure 16.   Simulated frequency response of the 6-4 operated in air. Frequency peak occurs at 2676 Hz.
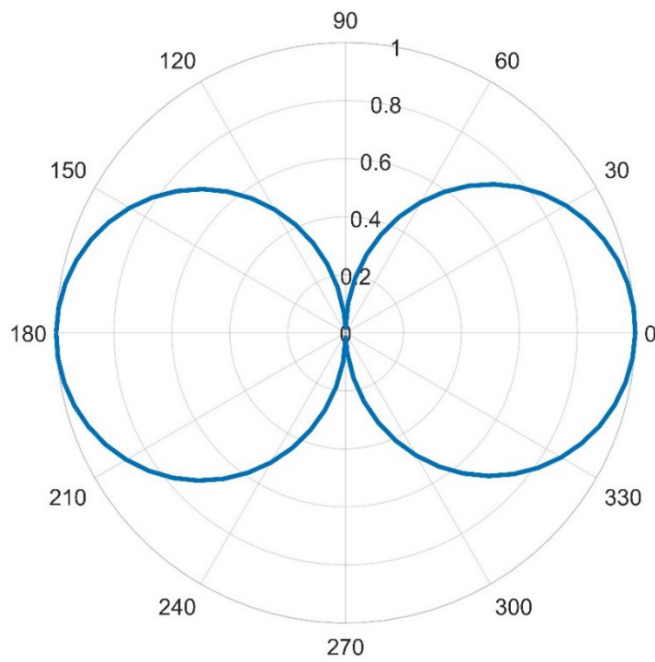
Figure 17.   Simulated normalized directional response of the 6-4 sensor operated in air at resonance (2676 Hz).

4.   Gen 6-4 Sensor in Oil

Figure 18 shows the simulated frequency response of the 6-4 sensor when operated in its underwater boot apparatus. The maximum displacement of the sensor is 13.58 nm. The operating fluid here is the PSF-1cSt instead of air. The simulated frequency peak occurs at 450 Hz, 5.88 times smaller than the simulated frequency peak in air. The bandwidth of the sensor at FWHM is also simulated to increase when operating in the silicone oil. Bandwidth increased to about 223 Hz; 2.9 times larger than the simulated air value of 77 Hz. Figure 19 shows the simulated normalized directional response of the 6-4 sensor when operated in oil.
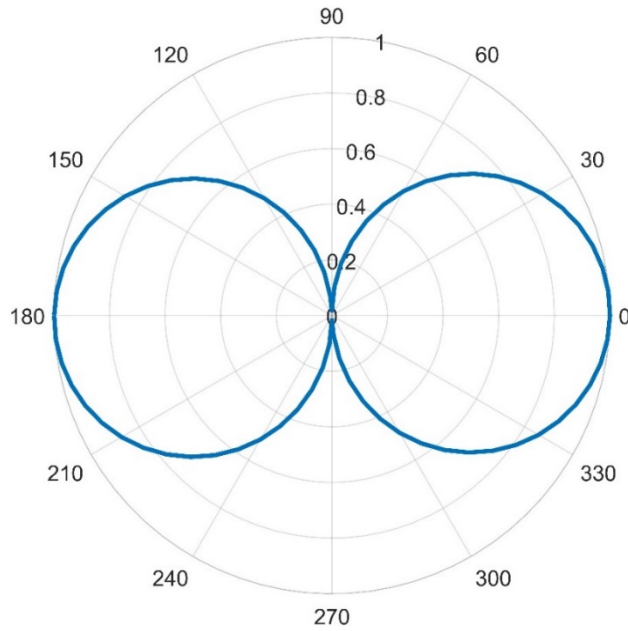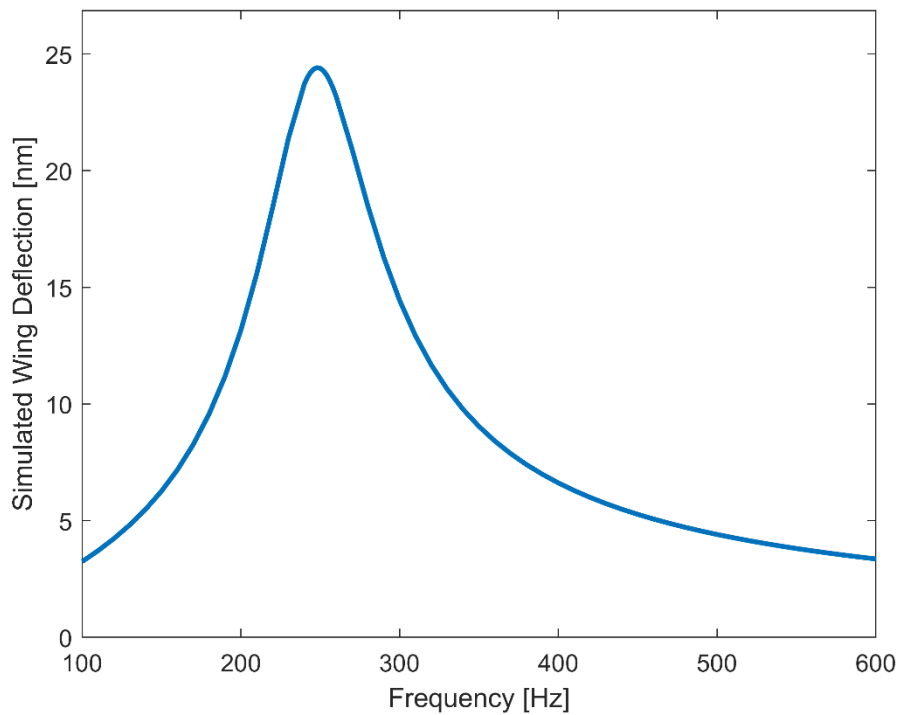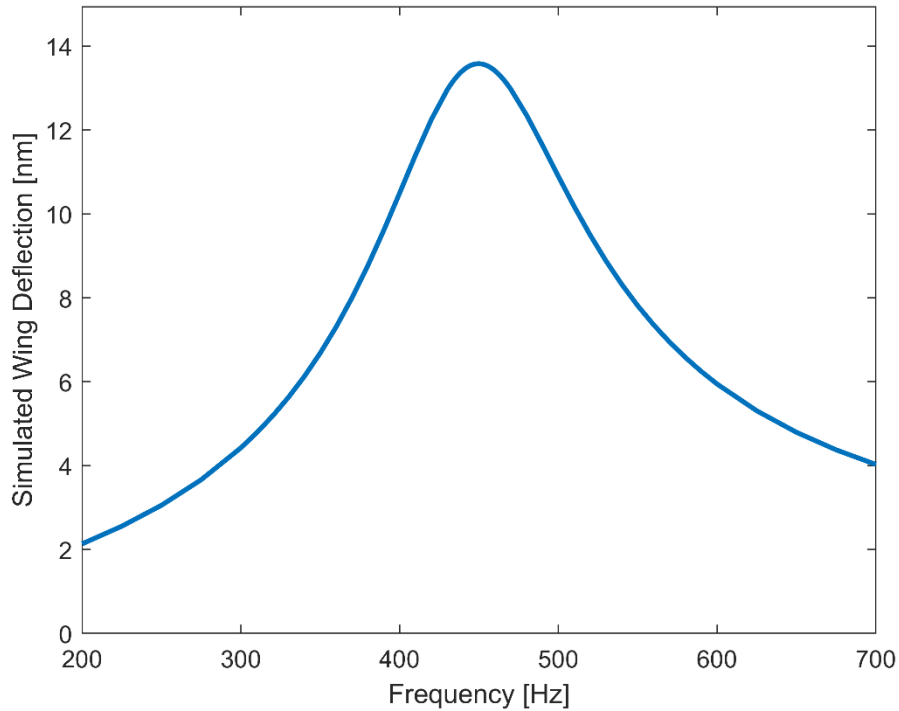

Figure 18.   Simulated frequency response of the 6-4 sensor in PSF-1cSt. Frequency peak at 450 Hz.
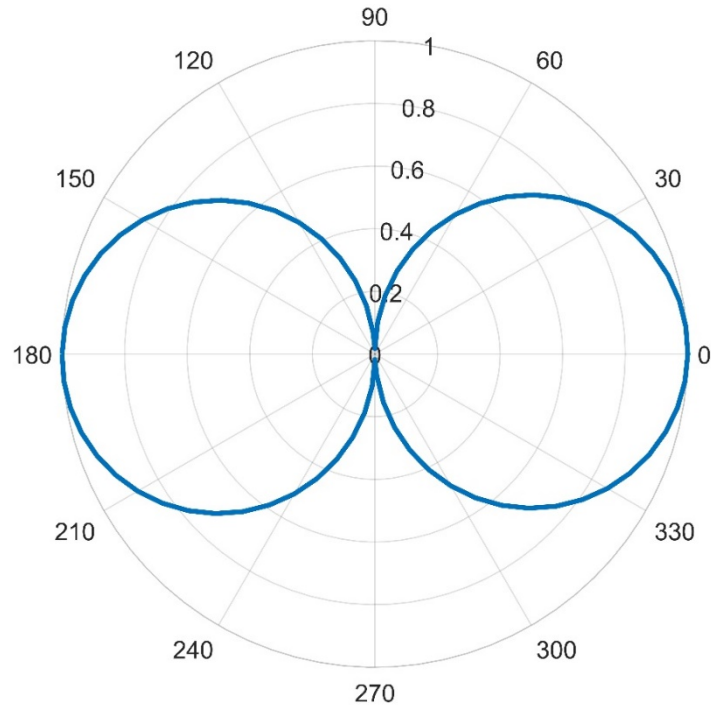
Figure 19.   Simulated normalized directional response of the 6-4 sensor in
PSF-1cSt. Response simulated at 450 Hz.

5.   Comb Finger Gap Optimization

The final simulation performed in COMSOL was an optimization of the gap between comb fingers used for the electronic readout using the 6-3 sensor operated in PSF-1cSt silicone oil. The original design of the 6-3 sensor has a gap width of 5 µm. It is desired to maximize the displacement of the comb fingers for a given sound pressure to generate the highest output voltage. The simulation was performed by adjusting the spacing between the comb fingers (from 2 µm to 10 µm), while setting the total number of comb fingers to fit the width of the sensor wing. Figure 20 shows the results of the optimization simulation.
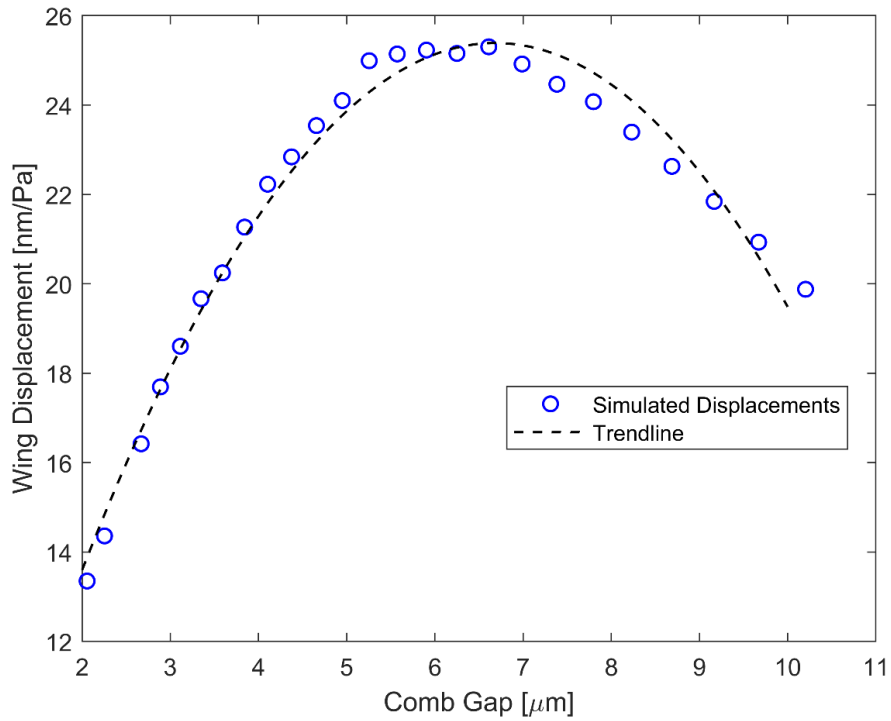
Figure 20.   Simulated displacement amplitude for the 6-3 sensor by varying
comb finger gap 2–10 µm.

The COMSOL optimization suggests that a channel gap between 5 µm and 7 µm will yield the maximum displacement amplitude for the 6-3 sensor. The peak displacement of about 25 nm/Pa corresponds to a 7 µm gap width. In practice, the narrower gaps are better because of the increased capacitance. Inside the 5–7 µm interval the optimal finger gap is 5 µm.

THIS PAGE INTENTIONALLY LEFT BLANK

III. ASSEMBLY AND EXPERIMENTAL SETUP

A. SENSOR AND READOUT CIRCUIT ASSEMBLY

The 6-3 and the 6-4 MEMS sensors are assembled the using the same process. In earlier studies, a commercial off the shelf capacitance-to-voltage converting integrated circuit (an MS3110) was employed. In this thesis, a newly designed readout electronic circuit by the Sensor Research Lab was employed to overcome the shortcomings of the previous approach. The sensor is attached to a printed circuit board (PCB) containing the readout electronics using a Norland Optical Adhesive 68 (NOA68) [25], a UV curable adhesive. The PCB is fabricated with a milled rectangular hole to expose the backside of the MEMS sensor to sound and a countersunk groove to provide a fixed location to set the sensor in place. The adhesive is applied to the countersunk region with a precision applicator and the sensor is placed onto the PCB. Figure 21 shows a cross-sectional diagram of the PCB with the sensor adhered to it. After the adhesive has cured, the sensor is electrically connected to the board using a wire bonder. Figure 22 shows the front and back side of a 6-4 sensor attached to a PCB.
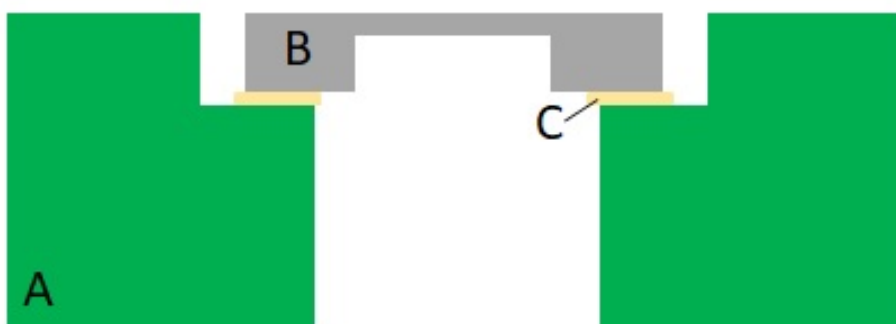
PC board (A) attached to the MEMS sensor (B) using UV cured adhesive (C).

Figure 21. Cross-sectional diagram of the sensor adhered to the board.
Adapted from [26].

The power to the electronics and output signal from the sensor are harnessed via a male HDMI-D connector, located at the base of the PCB. This connector is also used to

attach the PCB/sensor assembly to either a mount for air characterization or a boot housing for underwater characterization.

Figure 22.   Front (left) and back (right) of a 6-4 sensor attached to a PCB using NOA68 adhesive.

B.   SENSOR ASSEMBLY FOR TESTING IN AIR

For characterization in air, the PCB is attached to a 3D printed mount and held in place with a plastic screw. A female HDMI-D to female HDMI-A cable is connected to the circuit board at the HDMI-D end. At the HDMI-A end, an HDMI-A to 20-pin connector is attached. The mount used for characterization is shown in Figure 23. The 20-pin connector is connected to the direct current (DC) power supply and MFLI Lock-In Amplifier using the layout shown in Figure 24.
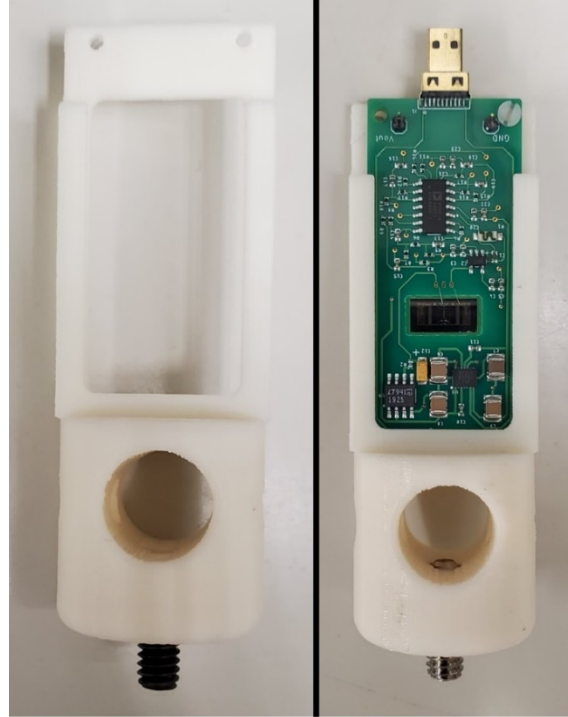
Figure 23.   3D printed mount used for characterization in air (left) and mount with sensor and PCB attached (right).
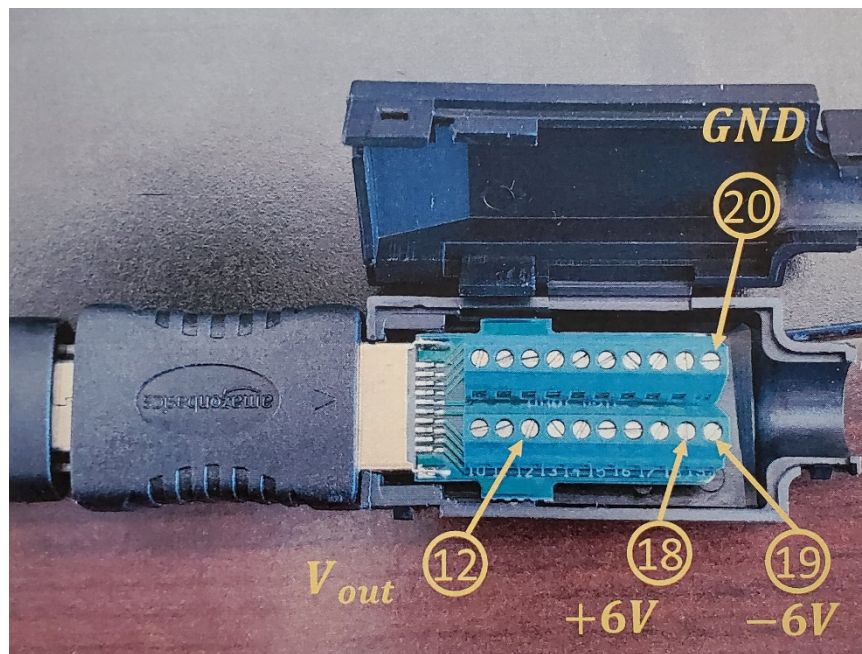
Figure 24.   Layout of the HDMI-A to 20-pin connector. V_{out} is the sensor output.

## C.	AIR CHARACTERIZATION SETUP

The schematic test setup used for characterization in air is shown in Figure 25. Measurements were performed in an anechoic chamber located at NPS. The mounted sensor is attached to an externally controlled turntable, which allows for directional characterization of the sensor. A PCB Piezotronics, model 378A21 reference microphone (sensitivity: 11.26 mV/Pa) [27] is attached in the circular hole of the sensor mount during frequency response measurements to eliminate any inconsistencies produced by the sound source. The reference microphone is removed during directional measurements to facilitate the rotation. The 378A21 is powered by a PCB Piezotronics, model 482C16 signal conditioner [28]. The DC power supply to the MEMS sensor is an Agilent Technologies E3620A dual-output power supply [29]. The "+VDC" and "-VDC" terminals are both set to a magnitude of six volts.
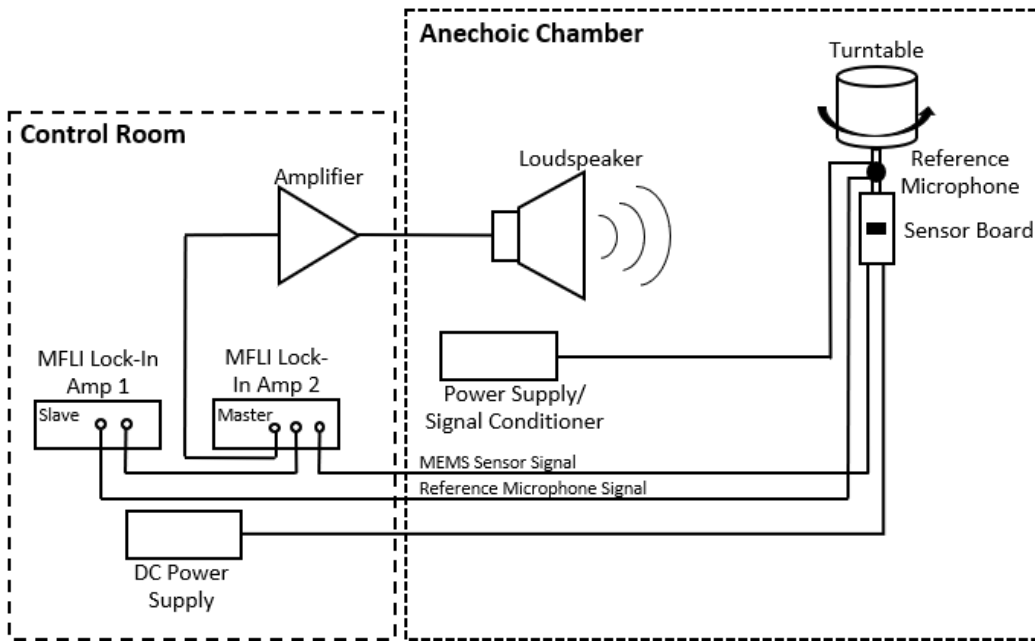
Figure 25.	Schematic diagram of the test setup in the anechoic chamber at NPS. Adapted from [26].

Figure 26 shows the physical layout of the sensor assembly and speaker used for generating sound inside the anechoic chamber. The minimum separation between the sensor and speaker was determined using the far-field equation [30] given in Equation (3.1)

$$d > \frac{\pi a^2}{\lambda}$$

(3.1)

where d is the distance between the source and sensor, λ is the wavelength of the highest measured sound frequency (this is the most limiting corresponding wavelength) and a is the radius of the speaker. The speaker has a radius of 3" (7.62 cm) and the maximum expected frequency is 3 kHz ($\lambda = 11.43$ cm). From Equation 3.1, the minimum separation between the speaker and MEMS sensor must be about 16 cm. Testing was performed in the anechoic chamber with a separation distance of 215 cm, satisfying the far-field requirement.
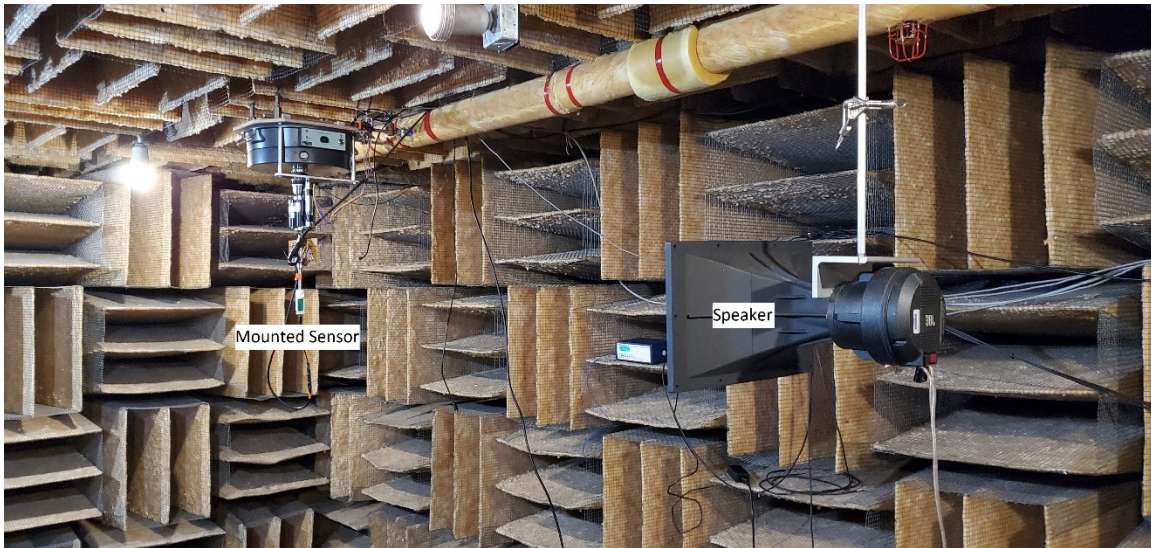
Figure 26.   Layout of the speaker and sensor assembly in the anechoic chamber.

D.   SENSOR ASSEMBLY FOR TESTING UNDERWATER

For underwater characterization, the PCB/sensor is attached to a housing, assembled at the Sensor Research Lab at NPS, using commercial off-the-shelf components.

The housing structural components consist of vacuum components corresponding to the 1.5-inch diameter standard size, purchased from the Kurt J. Lesker Company. The components consist of an aluminum half nipple, an aluminum centering ring (with a fluorocarbon O-ring), an aluminum flange blank, and a stainless-steel chain clamp. The flange blank is drilled and internally threaded using an M16x1.00 mm tap. A waterproof female HMDI-D to HDMI-D passthrough connector is threaded into the backside of the flange blank. The PCB HDMI-D connector is connected to the internal side of the waterproof passthrough connector. Figure 27 shows the individual structural components used to construct the underwater housing.
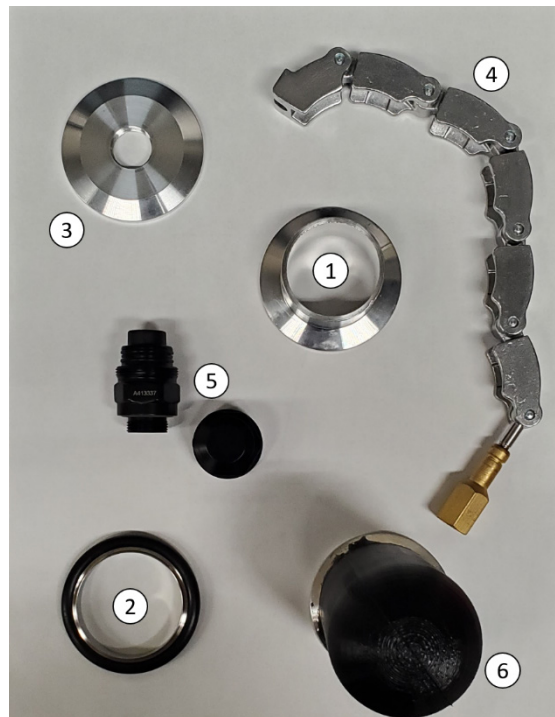
Half-nipple (1), centering ring (2), flange blank (3), chain clamp (4), passthrough connector and cap (5), and boot attached to half nipple (6).

Figure 27.   Structural components used for the underwater housing.

A boot made from PMC-780 is attached to the half nipple using Flexane-80 as an adhesive. The boot was molded to have an internal diameter of 1.5" using the process described by Espinoza [17]. Flexane was chosen due to its combination of strong adhesion

between aluminum and PMC-780 as well as flexibility under the stresses imposed by the chain clamp. Figure 28 shows the final steps for assembling the underwater housing with a sensor.

Before inserting sensor into housing (left). Fully assembled sensor in the underwater housing (right). Not shown: addition of the PSF-1cSt silicone oil.

Figure 28.   Final assembly step of the underwater housing.

E.   UNDERWATER CHARACTERIZATION SETUP

The underwater characterization was performed using the water tank at NPS. The sensor assembly is connected to the testing equipment using a waterproof HDMI-D to HDMI-A cable. The same HDMI-A to 20-pin connector used for the air characterization is used for the underwater characterization. Figure 29 shows the diagram for the underwater characterization test layout.
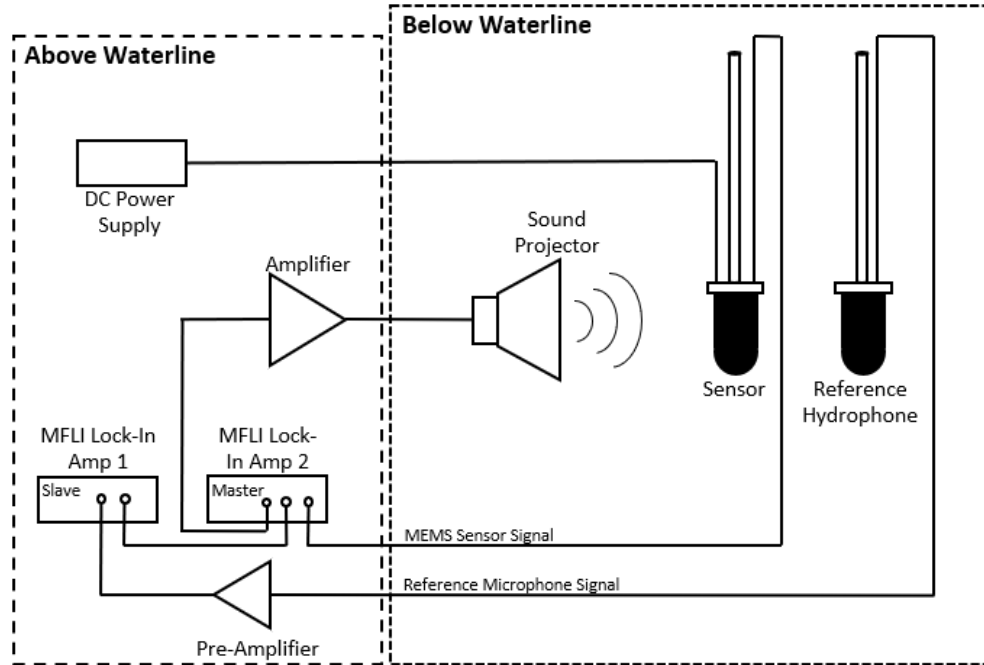
Figure 29.   Schematic diagram of the underwater test setup.

A B&K 8103 omnidirectional hydrophone (26.61 µV/Pa) [31] is used as a reference for frequency measurements. Appendix A lists the specifications of the B&K 8103 used for this research. The reference hydrophone is enclosed in an underwater housing similar to that of the sensor to replicate the sound environment the sensor operates in. The hydrophone is used in order to eliminate artifacts created by the underwater projector. The reference hydrophone output is passed to a Stanford Research Systems, model SR560 Amplifier (labelled pre-amplifier) [32] and then to the MFLI Lock-In Amplifier. The sound projector is an Electro-Voice, model UW30 underwater loudspeaker [33]. The sound projector is powered by a Hewlett-Packard HP467A power amplifier (labelled amplifier) [34]. Settings for the SR560 and the HP467A are outlined in Appendix B. The specifications of the UW30 loudspeaker are detailed in Appendix C. The same Agilent Technologies, model E3620A power supply is used to power the sensor for underwater testing. The power supply settings for the sensor were also the same as that used in the characterization in air.

Figure 30 shows the physical layout of the test setup in the water tank. Using Equation 3.1, the far-field distance can be calculated for underwater testing. The speaker

radius is 4.125" (10.48 cm) and the maximum expected frequency is 600 Hz (λ = 57.17 cm). The minimum separation distance, d, to maintain the far-field assumption in the underwater chamber is 1.38 cm. Testing was conducted with a separation distance of 28 cm.
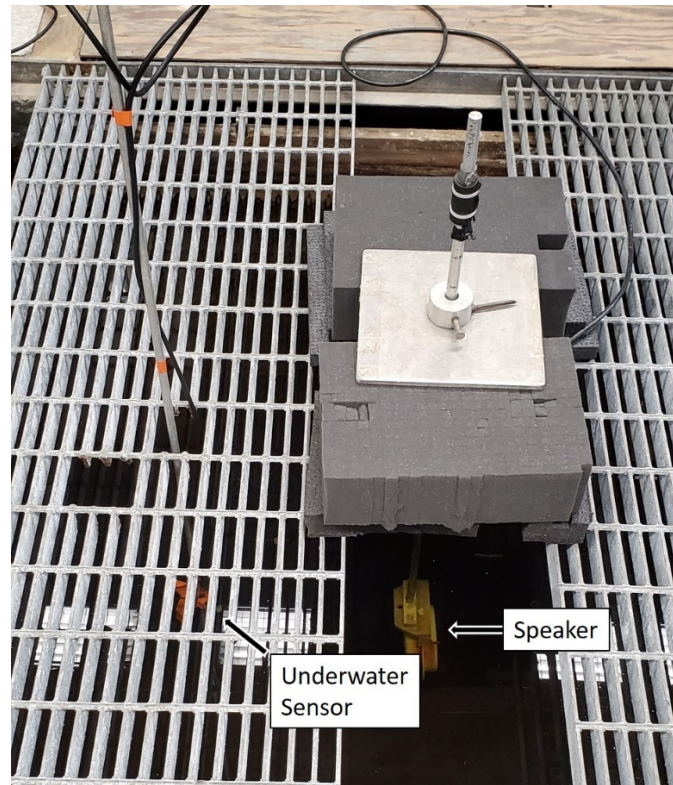
Figure 30.   Physical layout of the underwater test setup.

THIS PAGE INTENTIONALLY LEFT BLANK

IV. MEASUREMENTS AND RESULTS

A. CHARACTERIZATION IN AIR

The frequency and directional responses of the generation 6-3 and 6-4 sensors were measured in the anechoic chamber at NPS. Figure 31 shows the experimental and simulated frequency response of the 6-3 sensor. The bending resonance peak for the 6-3 sensor occurs at approximately 1487 Hz. The bandwidth at FWHM is about 88 Hz. The experimental and simulated directional responses are shown in Figure 32. The experimental response closely agrees with the simulated response. The close agreement of the experimental and simulated sensor characteristics indicates accuracy of the developed COMSOL model.
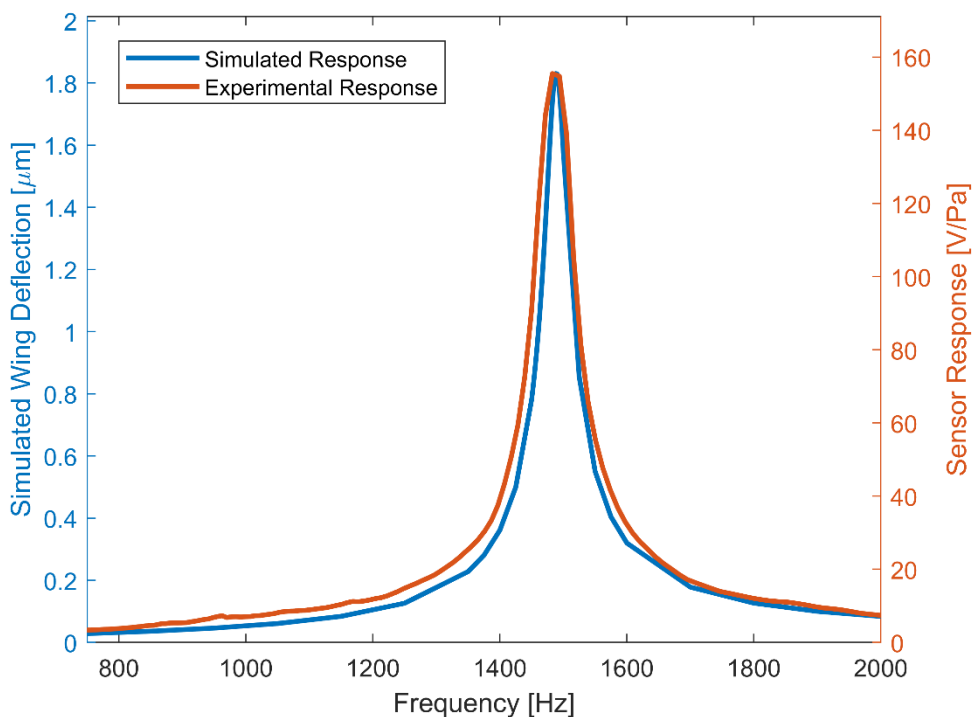
Figure 31.   Simulated and measured frequency responses for the 6-3 sensor in air.
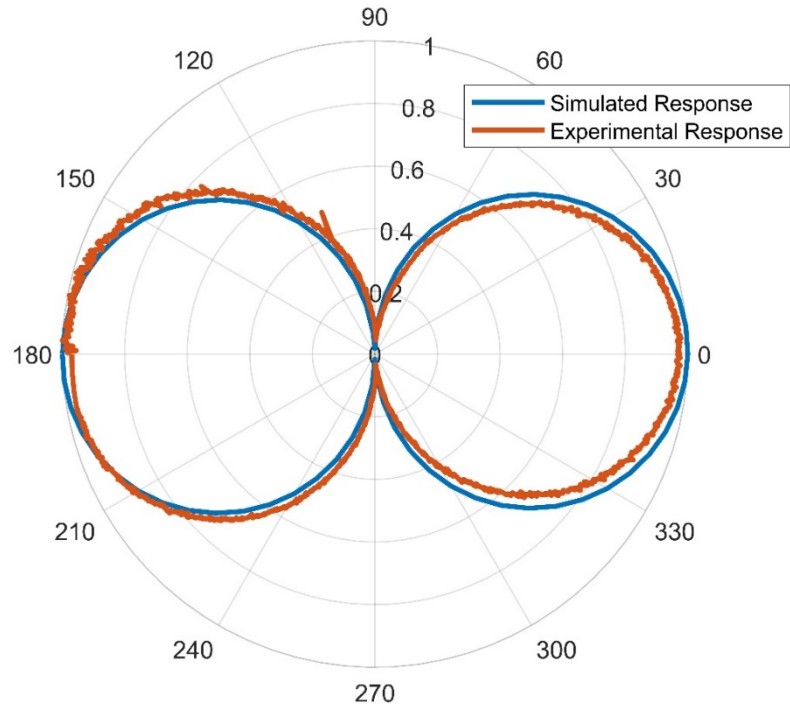
Figure 32.   Normalized directional responses (measured and simulated) of the
6-3 sensor in air.

Figure 33 shows the measured and simulated frequency responses for the 6-4 sensor. The measured frequency peak occurs at 2665 Hz with a bandwidth at FWHM of about 90 Hz. As with the 6-3 sensor, the experimental response closely agrees with the simulated response for the 6-4 sensor. For both sensors, the small difference in frequency peak and bandwidth can be explained by small variations in the sensor dimensions from that of designed due to manufacturing processes. The measured and simulated directional response is shown in Figure 34.
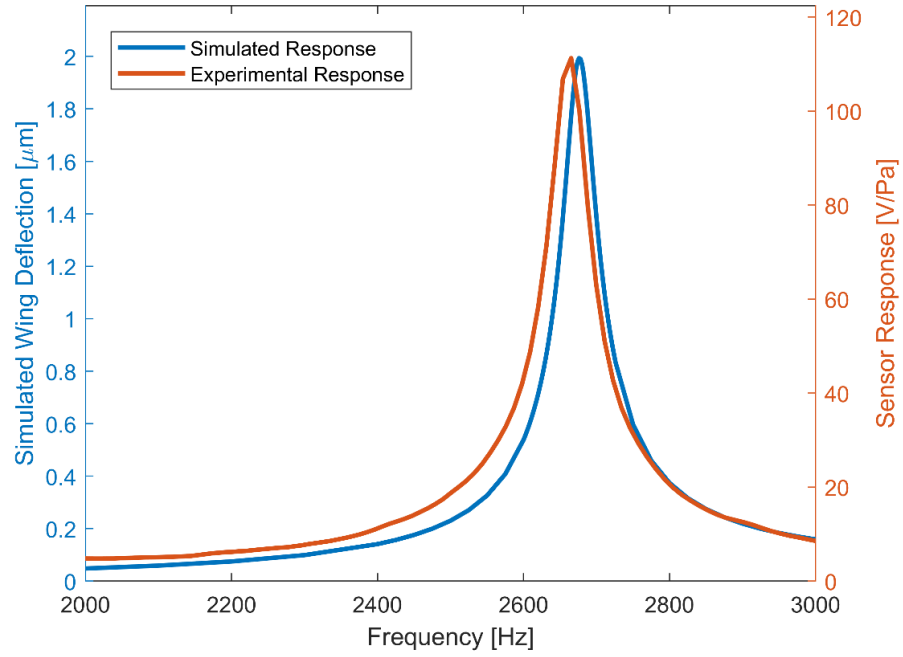
Figure 33.   Simulated and measured frequency responses of the 6-4 sensor in air.
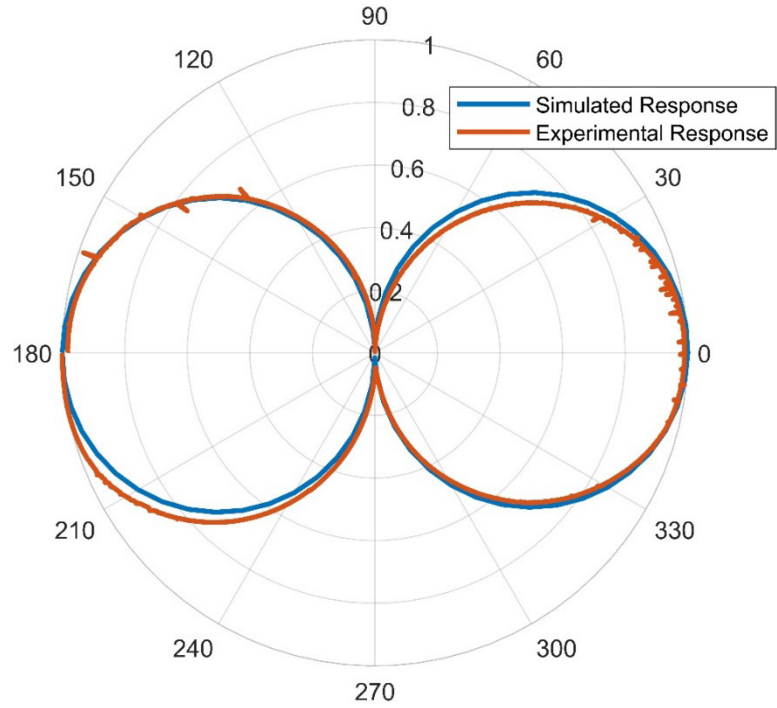
Figure 34.   Normalized directional responses (measured and simulated) of the 6-4 sensor in air.

B.   UNDERWATER CHARACTERIZATION

1.   Gen 6-3 Sensor

Initial underwater testing of the Gen 6-3 sensor did not match with the expected behavior based upon previous generations of the sensor developed at the Sensor Research Lab. The sensor exhibited higher sensitivity at its designed resonant frequency. It was expected to have a sensitivity of less than 1 V/Pa. Additionally, the bandwidth at FWHM was a fraction (~36 Hz) of the simulated value (~222 Hz). Figure 35 shows the measured frequency response of the Gen 6-3 sensor in underwater along with that of the simulation.
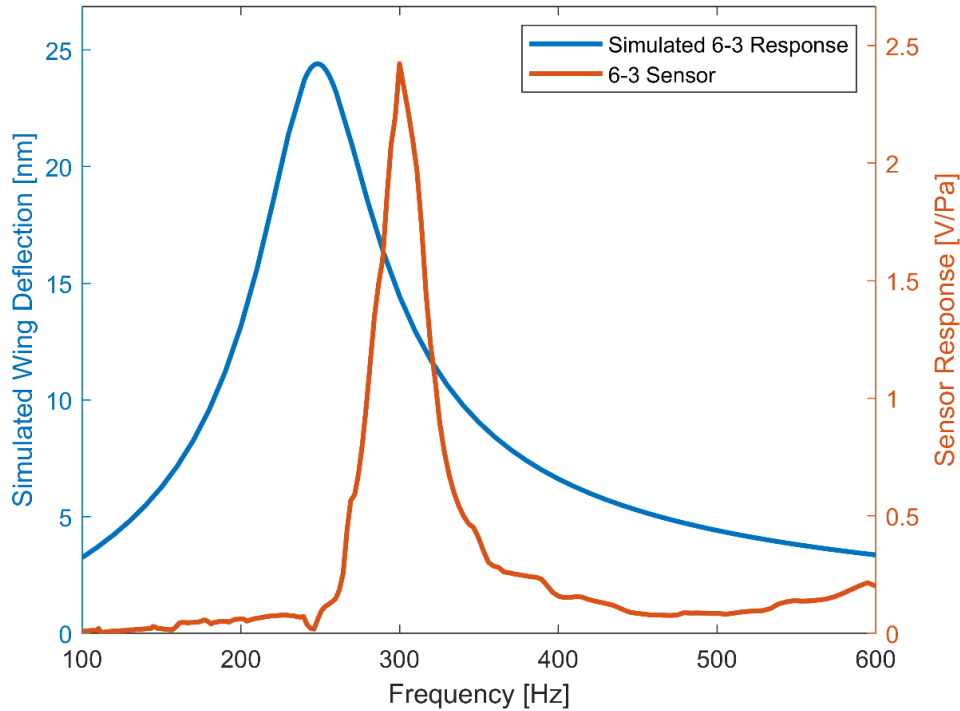
Figure 35.   Measured and simulated frequency responses of the 6-3 sensor underwater.

In addition, no clear directionality was observed as the 6-3 sensor was rotated in underwater. When operated at the resonant frequency of 300 Hz, the sensor was equally as responsive at normal sound incidence as it was when rotated 90° to the incident sound. From the poor directional response, it was suspected that the PCB containing the

electronics has a mechanical resonance at approximately 300 Hz. Similar effects were also noticed when characterizing the Gen 6-4 sensor. Mechanical resonances were observed across all tested frequencies and consistently resolving the frequency and directional response of the 6-4 sensor did not occur. Unexpected resonant modes were noticed at frequency multiples of 300 Hz and erratic directional response was achieved at all frequencies in between these resonant modes.

Two sources for this resonance were suspected. First, the location where the PCB mount into the surrounding structure was not rigid. Second, the boot used for housing the sensor assembly can resonate at its normal modes affecting both frequency and directional responses of the sensor. It was suspected that this effect was dependent of the thickness of the boot wall.

The loose connection between the PCB and the housing was corrected using a marine adhesive sealant [35] at the junction where the PCB HDMI-D connector is plugged into the passthrough connector (see item (5) in Figure 27). The sealant was built up so that it covered the entire HDMI-D connector and made contact with the PCB. Figure 36 shows the modifications made using the marine sealant. This modification was done to both Gen 6-3 and Gen 6-4 sensors. In addition, a 3 mm thick boot was also fabricated to assess the effect of boot thickness on the sensor characteristics.

Figure 36.   Gen 6 sensor assembly modified with marine sealant.

2.   Underwater Characterization Using a 5 mm Thick Boot

With the connection point between the PCB and the passthrough connector better supported, a comparison of the sensor response between using a 5 mm thick boot and a 3 mm thick boot could be conducted. This would determine any effects the boot thickness had on the sensor characteristics. Testing was conducted at the water tank at NPS for both the 6-3 sensor and the 6-4 sensor. Directionality was assessed at 45° intervals from 0° to 360° via hand-positioning of the sensor. Bearing accuracy was assessed to by ±5°. Figure 37 shows the frequency response of the modified Gen 6-3 sensor, encased in a 5 mm thick boot, at normal sound incidence compared to the COMSOL modeled response.

Figure 37.　Comparison of measured and COMSOL simulation of Gen 6-3
sensor frequency responses using a 5 mm thick boot.

The simulated peak response for the 6-3 sensor occurred at 248 Hz. The experimental response occurred at 292 Hz. The peak amplitude is 0.93 V/Pa, which is consistent with previous generations of sensors developed at the Sensor Research lab at NPS. The frequency peak at ~120 Hz is attributed to mechanical resonance for the 6-3 sensor. The bandwidth at FWHM is about 45 Hz, which is smaller than the simulated response of the sensor. It is suspected that the PCB still oscillates at ~300 Hz but the mechanical resonance is considerably more damped by the marine sealant. Directionality at resonance still could not be achieved; however, off-peak directional response was achieved in a small frequency range beyond the resonant peak. Figure 38 shows the frequency response, in 45° increments, for the Gen 6-3 sensor with the 5 mm thick boot.
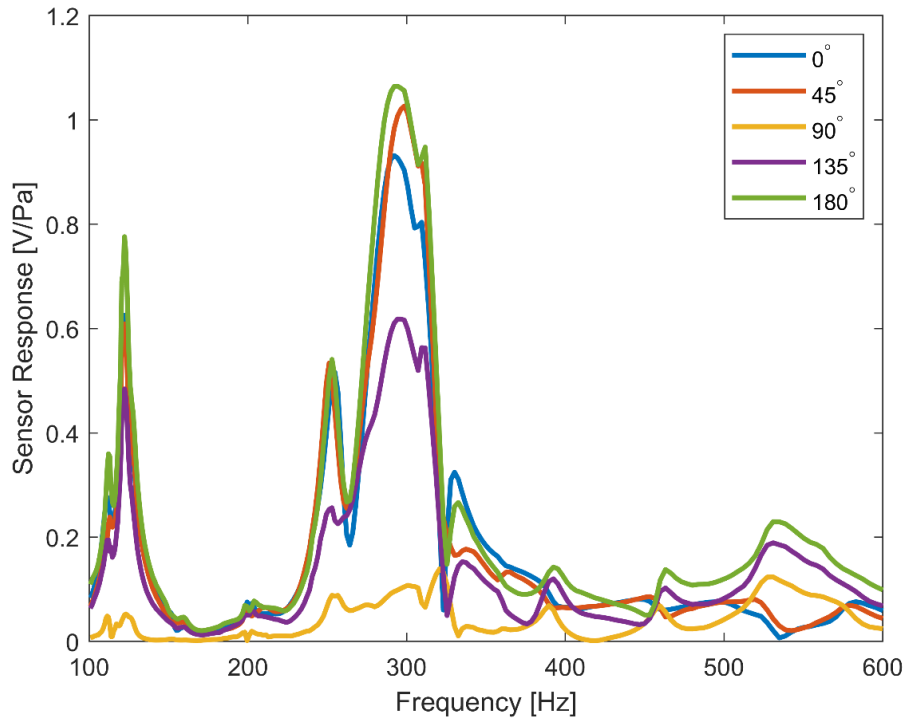
Figure 38. Gen 6-3 sensor frequency response in 45° increments with 5 mm boot thickness.

At resonance (300 Hz), the marine sealant successfully damped the mechanical oscillations when the sound is incident at 90°, as seen in Figures 38 and 39. The sensor inconsistently indicated directionality when measured at angles between the normal and 90° at resonance; however, the frequency range between 335 Hz and 375 Hz exhibited consistent directionality. Figure 39 shows the directional response of the Gen 6-3 sensor at the off-peak frequency of 355 Hz.

Figure 39.   Normalized directional response of the Gen 6-3 sensor with a 5 mm boot thickness measured at 355 Hz.

At 355 Hz, the 6-3 sensor shows expected directional response to the sound source. The 90° to 270° lobe (backside lobe) has 84% of the response of the 270° to 90° lobe (frontside lobe).

The Gen 6-4 sensor also exhibited improved response with the addition of the marine sealant. A peak resonance range occurred between 468 Hz and 534 Hz. Figure 40 shows the frequency response of the modified Gen 6-4 sensor, encased in a 5 mm thick boot, at normal incidence of sound compared with the COMSOL simulated response.
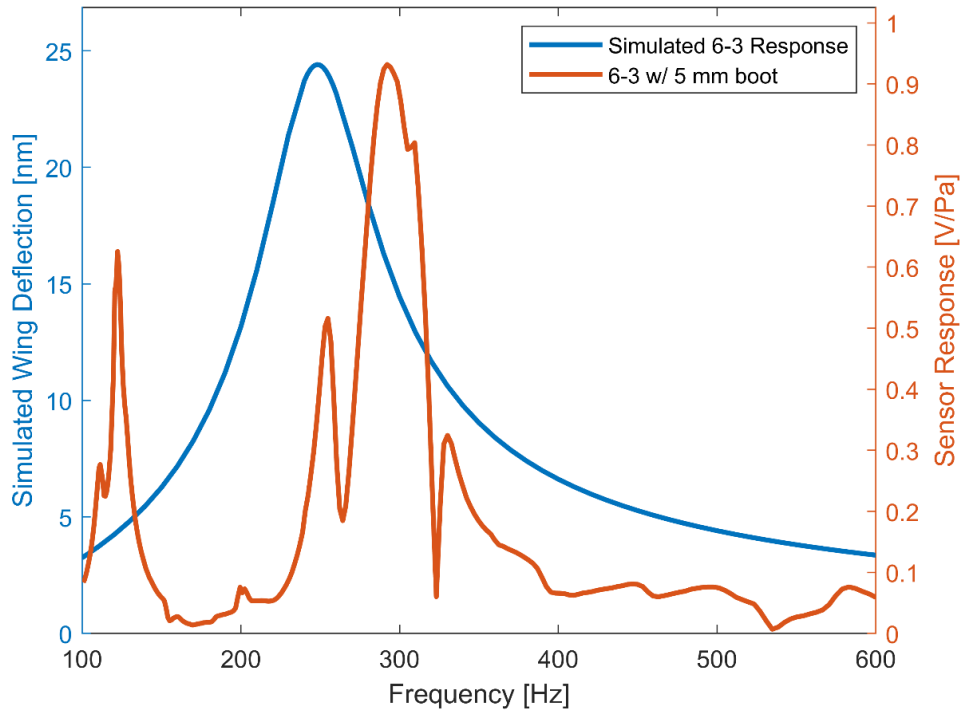
Figure 40.   Comparison of measured and simulated Gen 6-4 sensor responses
using a 5 mm boot.

The simulated peak response for the Gen 6-4 sensor occurred at 450 Hz while the measured response showed a broad peak close to expected frequency response. The peak response amplitude reached approximately 0.16-0.20 V/Pa. The bandwidth of the 6-4 sensor was simulated to be approximately 223 Hz and measurement shows a bandwidth of about 144 Hz. Directional response was also achieved within the resonant frequency range. Figure 41 shows the frequency response, in 45° increments, for the Gen 6-4 sensor with the 5 mm thick boot.
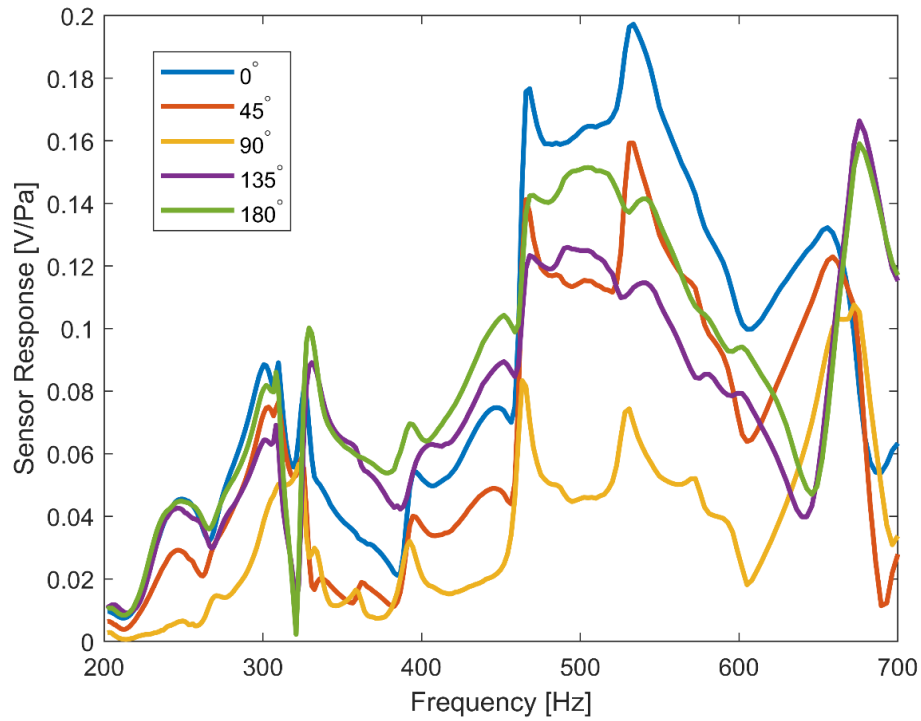
Figure 41.   Measured frequency response of Gen 6-4 sensor in 45° increments
with 5 mm thick boot.

The Gen 6-4 sensor showed directionality within the peak resonance region compared to that of the Gen 6-3 sensor. This can be attributed to the lack mechanical resonance of the assembly in the peak resonance region of the 6-4 sensor. Figure 42 shows the directional response of the Gen 6-4 sensor at an operating frequency of 500 Hz.
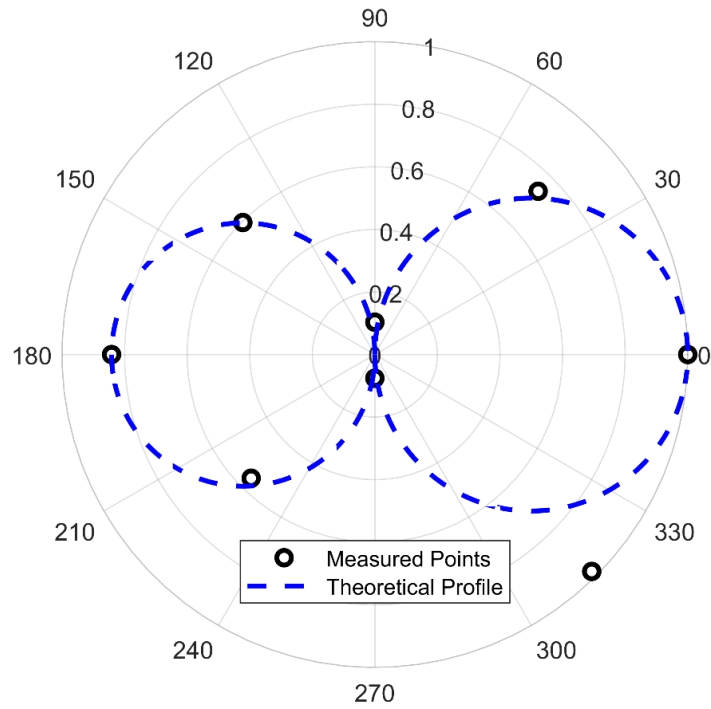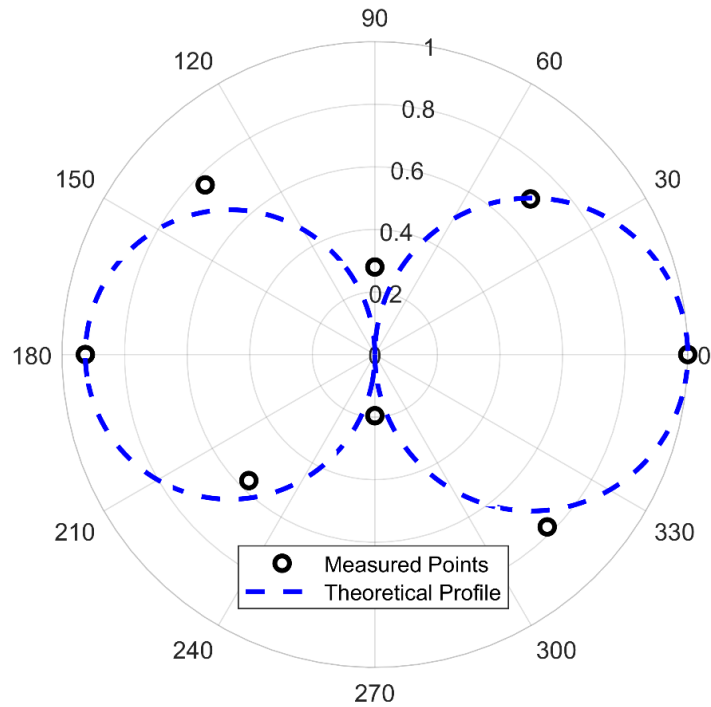
Figure 42.   Normalized directional response of the Gen 6-4 sensor with a 5 mm boot thickness measured at 500 Hz.

At 500 Hz, the Gen 6-4 sensor exhibits directional response close to that of the expected behavior. The backside lobe has 93% of the response of the frontside lobe.

3.   Underwater Characterization Using a 3 mm Thick Boot

For understanding the effects of boot thickness on frequency and directional responses, the 5 mm thick boot was exchanged for a 3 mm thick boot. The marine sealant modified Gen 6-3 and Gen 6-4 sensors were used in these experiments. Tests were conducted in the water tank at NPS. The Gen 6-3 sensor exhibited improved frequency response when the 3 mm thick boot was utilized. The resonant peak remained at 292 Hz, but the severity of the trough regions (see Figure 37) surrounding the resonant peak were reduced, confirming that the boot thickness had some effect on the response of the sensor. The sensitivity of the sensor also decreased to approximately 0.7 V/Pa. This can be attributed to a reduction in the mechanical oscillation of the boot near the sensor resonance. The bandwidth of the sensor increased to about 69 Hz. Figure 43 shows that the frequency

response of the modified Gen 6-3 sensor, encased in a 3 mm thick boot, at normal incident sound closely matches with that of the simulated response using COMSOL.
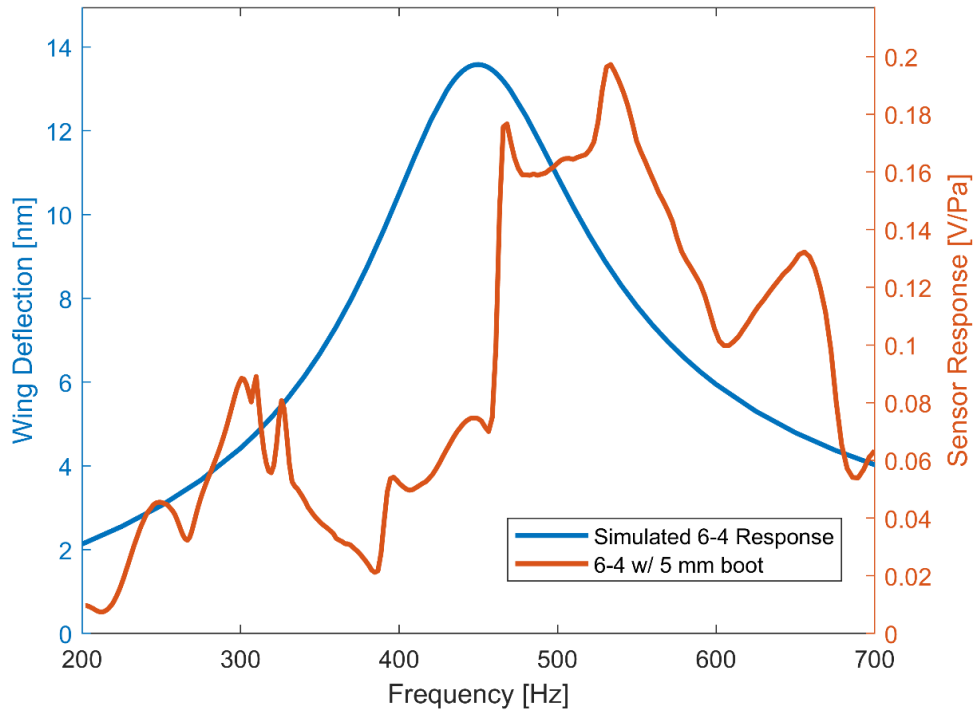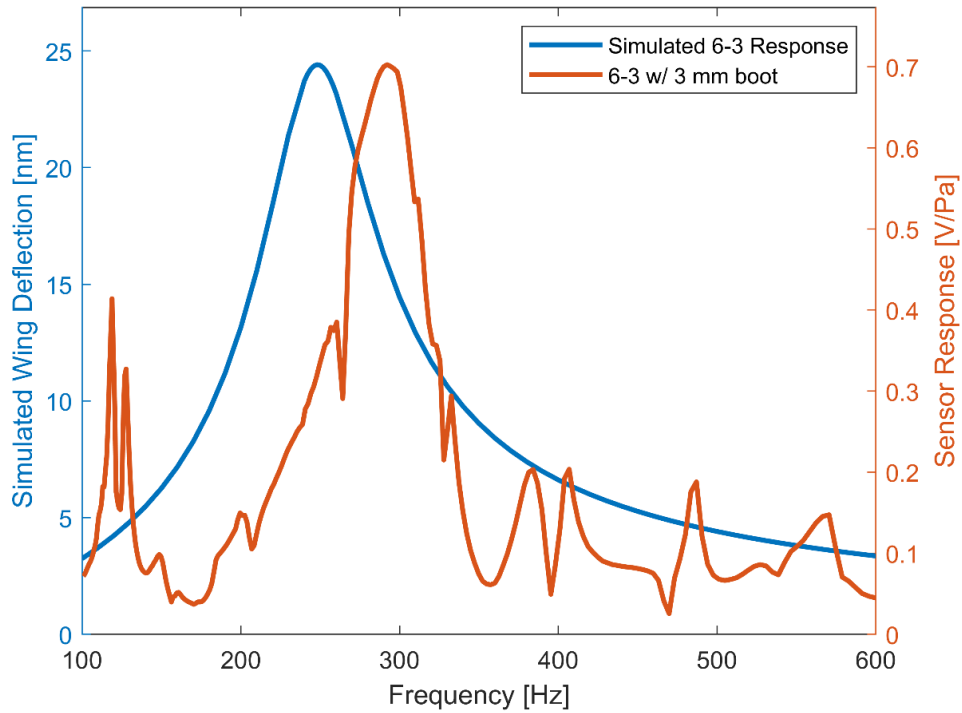

Figure 43.   Comparison of measured and simulated responses of the Gen 6-3 sensor using a 3 mm thick boot.

Directional response of the Gen 6-3 sensor was also measured using the 3 mm thick boot. Figure 44 shows the measured frequency responses, in 45° increments, for the Gen 6-3 sensor with the 5 mm thick boot.
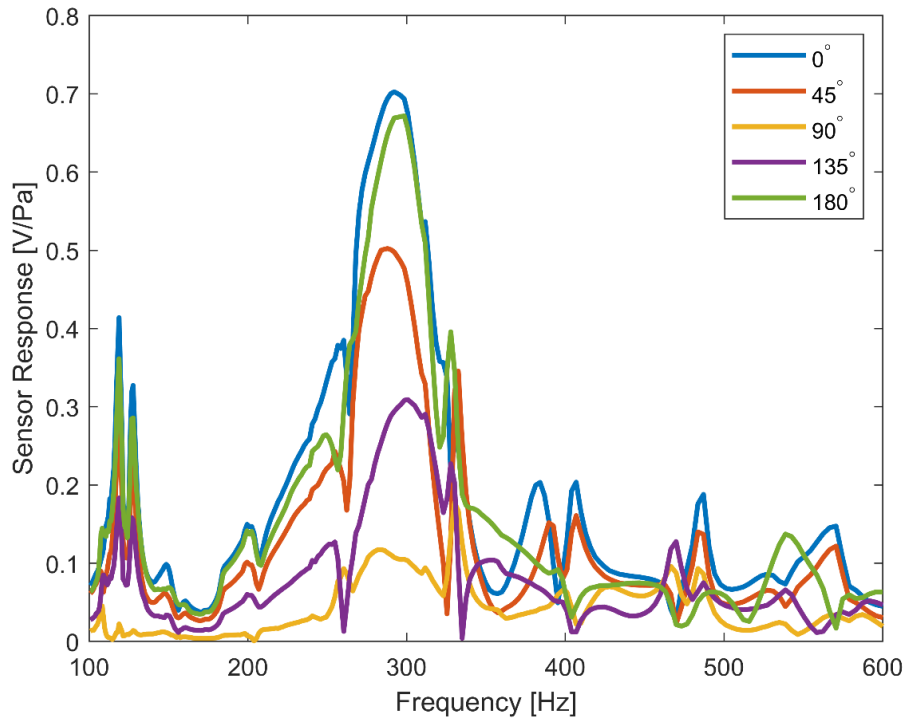
Figure 44.   Frequency responses of Gen 6-3 sensor in 45° increments with 3 mm thick boot.

Replacing the 5 mm thick boot with the 3 mm thick boot further reduced the impact of the mechanical resonance at 300 Hz. This reduction allowed for directional response to be achieved in the peak resonance region. Additionally, directionality is achieved across a wide range of frequencies for the Gen 6-3 as compared to the small range of frequencies achieved using the 5 mm thick boot. Figure 45 shows a polar plot of the directional response of the Gen 6-3 sensor at an operating frequency of 292 Hz.
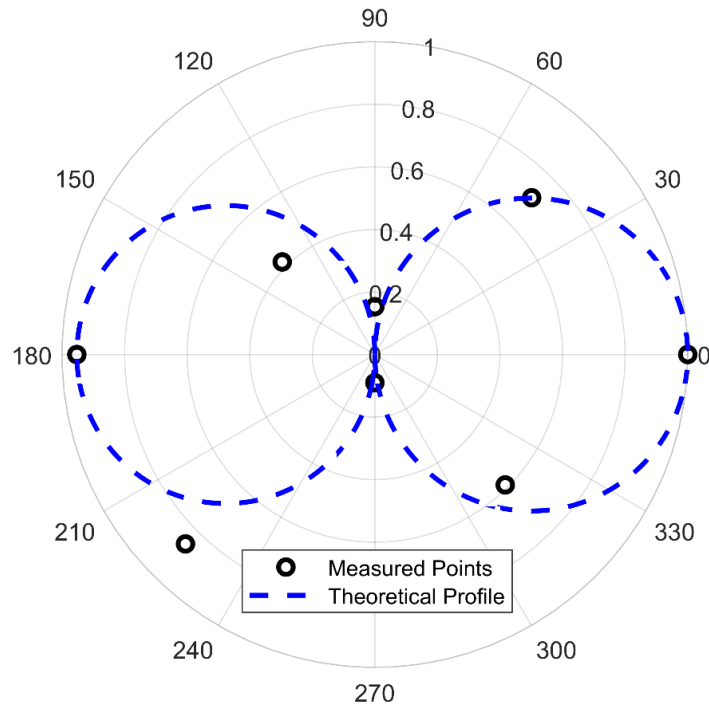
Figure 45.   Normalized directional response of the Gen 6-3 sensor with a 3
mm thick boot measured at 292 Hz.

At the peak resonance region, the Gen 6-3 sensor using the 3 mm boot thickness shows expected directional response to the sound source. Additionally, the backside lobe strength improved when compared to that of the 5 mm thick boot. The backside lobe response for the 3 mm thick boot was 95% of the frontside lobe response.

The Gen 6-4 sensor also showed improvement in frequency response when using the 3 mm boot thickness. The peak response range using the 3 mm thick boot occurs between 482 Hz and 567 Hz with response amplitude reaching 0.15-0.21 V/Pa. The bandwidth for this sensor is approximately 149 Hz. Figure 46 shows the frequency response of the modified Gen 6-4 sensor, encased in a 3 mm thick boot, at normal incident of sound compared with the COMSOL simulated response. The response shows that mechanical vibrations of the boot and circuit board is still present, which requires further optimization of the assembly.
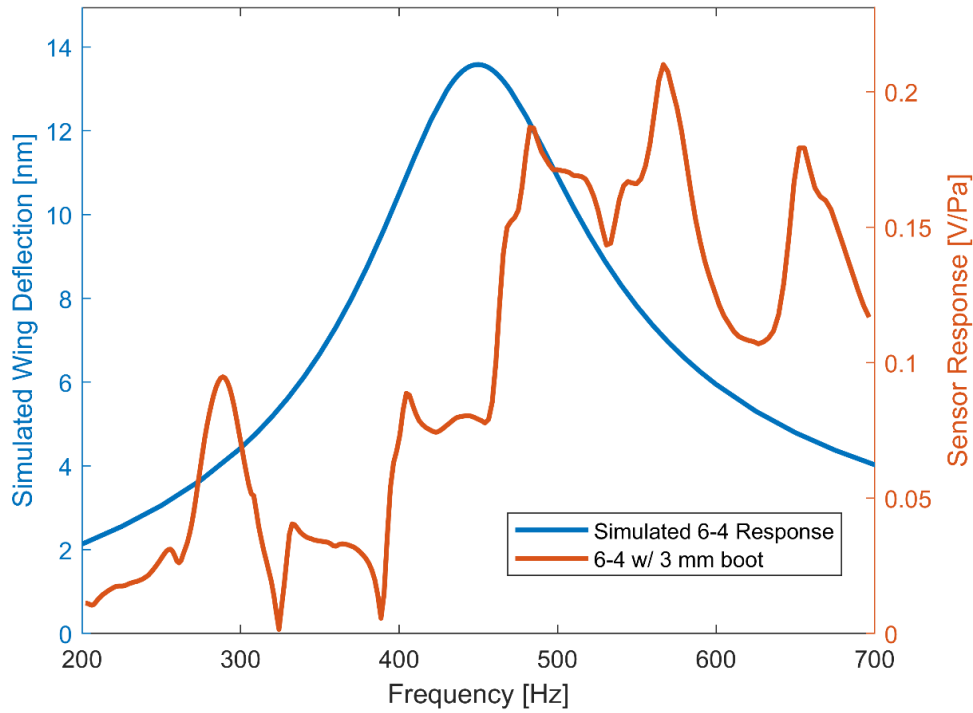
Figure 46.   Comparison of measured and simulated Gen 6-4 sensor responses
using a 3 mm thick boot.

Directionality for the Gen 6-4 sensor using the 3mm thick boot is exhibited across nearly the entire operating range of the sensor. Figure 47 shows the frequency responses, in 45° increments, for the Gen 6-4 sensor with the 3 mm thick boot. Figure 48 shows polar plot of the directional response of the Gen 6-4 sensor at an operating frequency of 523 Hz. Using the 3 mm boot thickness, the backside lobe response is found to be about 77% of the frontside lobe response.
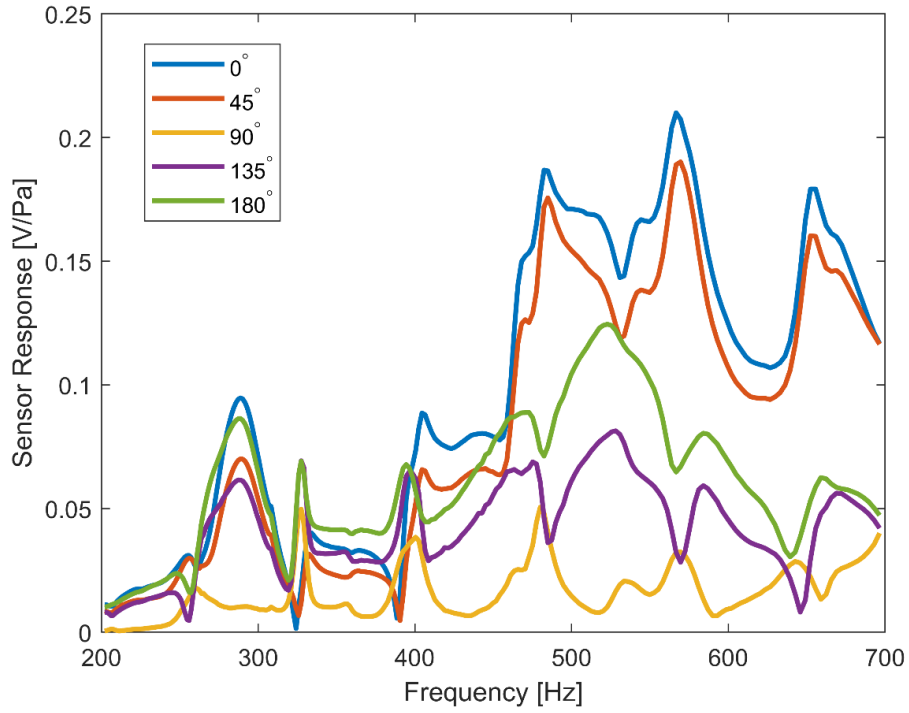
Figure 47.   Measured Gen 6-4 sensor frequency responses in 45° increments
with the 3 mm thick boot.
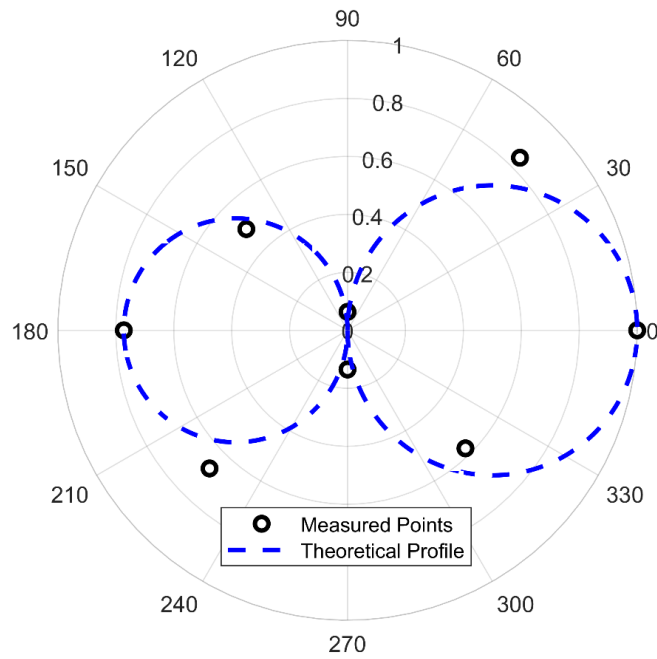
Figure 48.   Normalized directional response of the Gen 6-4 sensor with a 3
mm thick boot measured at 523 Hz.

4. Comparison of Responses for Different Boot Thickness

Figure 49 shows a comparison of the frequency responses for both boot thicknesses using the Gen 6-3 sensor. It can be seen that the Gen 6-3 sensor response improved with less mechanically induced oscillations using the 3 mm thick boot compared to that of the 5 mm thick boot. The peak response amplitude reduced from 0.93 V/Pa to 0.70 V/Pa, but the higher peak response was being driven by the mechanical oscillations of the PCB/boot combination at 300 Hz using the 5 mm boot. Additionally, the bandwidth of the sensor widened when using the thinner boot. Bandwidth increased from 45 Hz to 69 Hz.
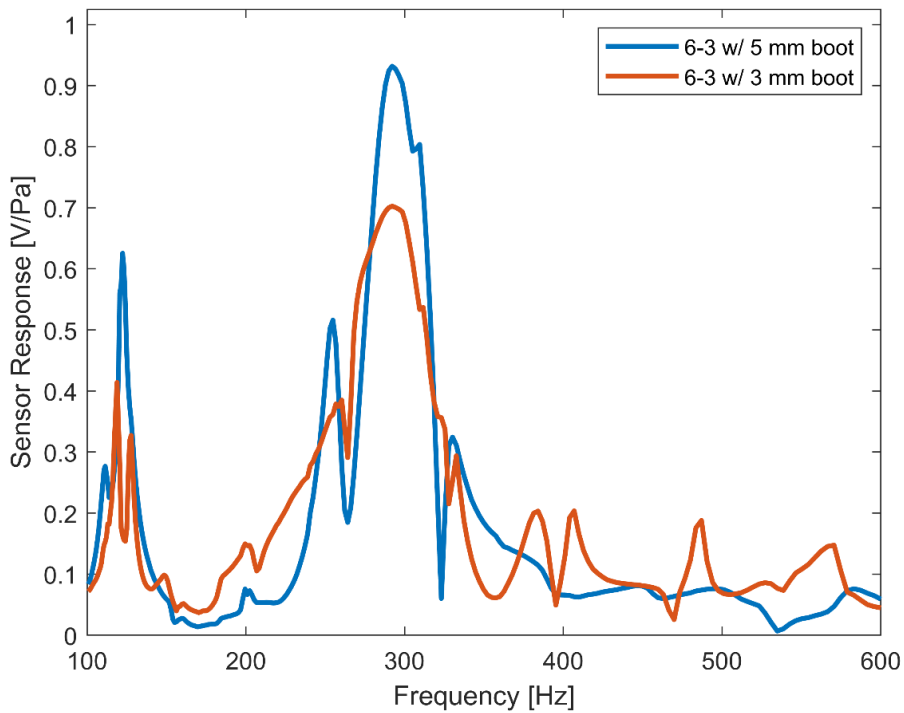
Figure 49.   Frequency responses of the Gen 6-3 sensor using the two boots
with different thicknesses.

Directionality could not be achieved in the peak region using the 5 mm boot, whereas it could be achieved using the 3 mm boot. Peak region directionality also allows for increased sensitivity of the sensor due to the increased response amplitude. Directional response could also be achieved in a wider range of frequencies when using the 3 mm boot.

The Gen 6-4 sensor performance also slightly improved when reducing the boot thickness to 3 mm. The peak response region widened from 468–534 Hz (66 Hz) to 482–567 Hz (85 Hz). Peak amplitude also increased from 0.2 V/Pa to 0.21 V/Pa. The bandwidth of the Gen 6-4 sensor also increased from 144 Hz to 149 Hz. Figure 50 shows a comparison of the frequency responses for both boot thicknesses using the Gen 6-4 sensor.
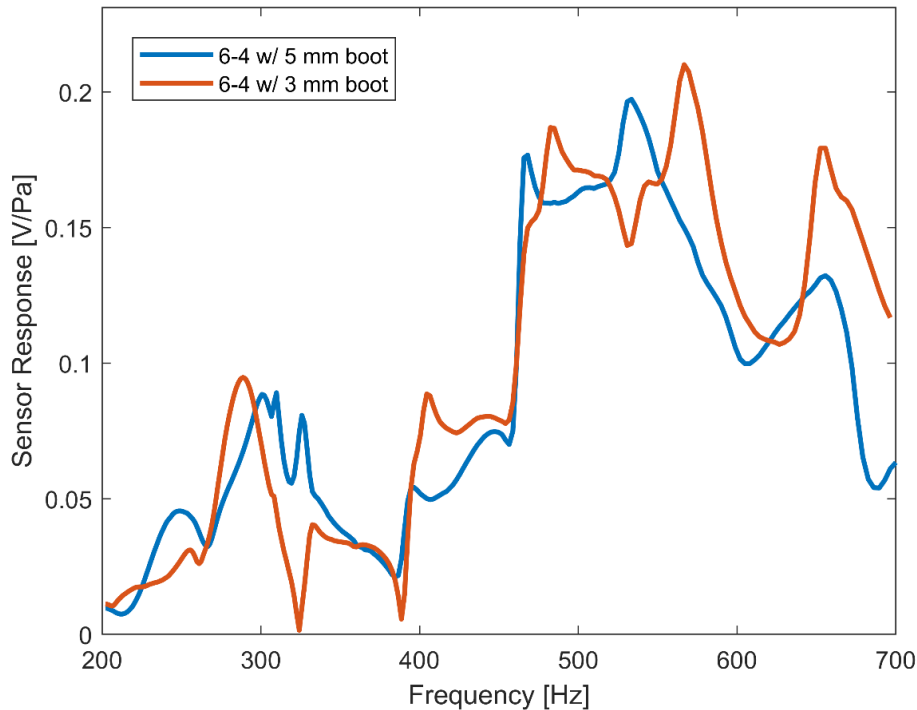
Figure 50.   Frequency response of the Gen 6-4 sensor using the two boot thicknesses.

The directional response amplitude of the Gen 6-4 sensor was largely unchanged by reducing the boot thickness; however, a larger range of frequencies exhibited consistent directionality in the 3 mm thick boot compared to the 5 mm thick boot. The results presented here show that the sensor performance is affected by both the circuit board used for integrating it with readout electronics as well as the housing used for underwater operation. The two sensors employed showed that the frequency of detection can be tuned by adjusting the mechanical parameters of the sensor. The measured directivity patterns

51

show that the MEMS based sensors can be used for determining bearing of sound with wavelengths much larger than the sensor dimensions.

V. CONCLUSIONS

A. SUMMARY OF RESULTS

In this thesis, the performance of two MEMS directional sensors was characterized both in air and underwater environments. In addition, sensor characteristics were simulated using COMSOL Multiphysics finite element modeling software and compared with the measurements. The two MEMS sensors were designed to have their bending resonant modes at 300 Hz and 520 Hz when operated in underwater environment. The characterization of the sensors in air was found to have the expected resonant frequencies and directional responses. For underwater operation, sensors were housed in a custom-made boot containing silicone oil that has acoustic impedance close to that of the water.

Challenges were presented when performing the underwater characterizations, but were overcome via revisiting the structural components of the housing used for underwater packaging of the sensor. A structural housing to protect the sensor from the environment is required for any sensor operation to occur. The underwater housing of the MEMS acoustic sensor presents additional challenges in reducing vibrational influence on the sensor readings. Robust structural support and analysis of mechanical vibrational modes is critical to the high-fidelity operation the MEMS acoustic sensor in an underwater environment. Finally, a directional MEMS acoustic sensor was shown to be viable path for further exploration into new Navy acoustic sensors.

The development of new acoustic sensor technology is critical to maintaining dominance in the undersea operating environment. Higher sensitivity sensors allow for platforms to detect and mitigate threats earlier and potentially before counter-detection occurs. Smaller form factor sensors allow for an increase in the number of employed sensors, improving the durability of platforms, allowing them to sustain more damage and operate longer. The benefit of a low-cost, low-profile, directional MEMS based acoustic sensor is critical to continuing the dominance of the U.S. Navy at sea.

B. RECOMMENDATIONS FOR FUTURE WORK

The COMSOL simulation accurately predicts the behavior of the Gen 6-3 and Gen 6-4 sensors in air. Further refinement to the model is required to increase the accuracy with respect to the sensor response underwater. Additional simulation modifications to include the surrounding underwater housing will be necessary to reduce any discrepancies between the simulation and experimental results.

Furthermore, identification and elimination of mechanical resonance modes from the housing/circuit board is critical to measuring intrinsic performance of the sensor. Simulation of the underwater housing resonant frequencies, both with and without the sensor, would need to identify these resonant modes. Then, additional measures can be implemented to minimize or shift the resonance out of the region where the sensor is most likely to respond. Modifications to the structural mating of the PCB and housing showed improvement in reducing mechanical resonances. Further structural changes to the PCB and to how the PCB is secured inside the housing are necessary for improved sensor performance.

The underwater testing facility at NPS is not designed for testing at the frequencies that the MEMS based sensors are designed for. Interference from the testing environment could not be entirely eliminated and contributed additional artifacts in the experimental data. Verification of these results at a facility designed to operate at low frequencies should be conducted to confirm these findings.

This research simulated an optimum comb finger spatial density to maximize sensor output. Experimental verification of the simulation is needed to ensure that the model is robust.

Finally, the operating fluid used in the underwater housing could be improved to more closely match the acoustic impedance of the surrounding underwater environment. Additionally, the operating fluid is not something commonly found on Naval platforms. Use of a non-conducting medium is required to prevent electrical shorting of the sensor inside the underwater housing. An alternative operating fluid, such as de-ionized water, could be explored.

APPENDIX A. B&K 8103 REFERENCE HYDROPHONE SPECIFICATIONS

This appendix provides the manufacturer specifications for the B&K 8103 reference hydrophone used in this research [31].

Sensitivity: -211.5 dB re 1V/μPa, 26.61 μV/Pa

Dimensions:
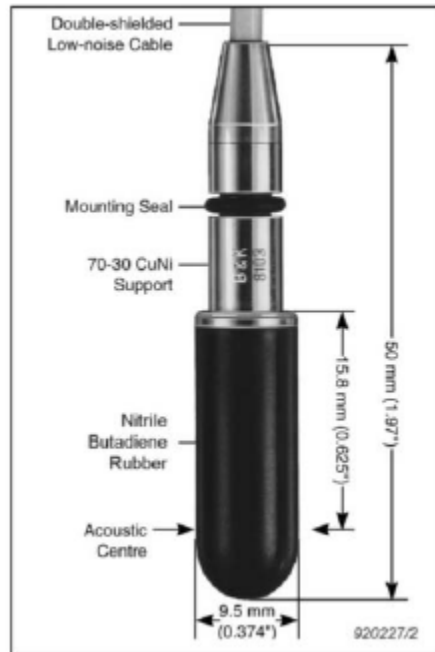
Frequency Response:
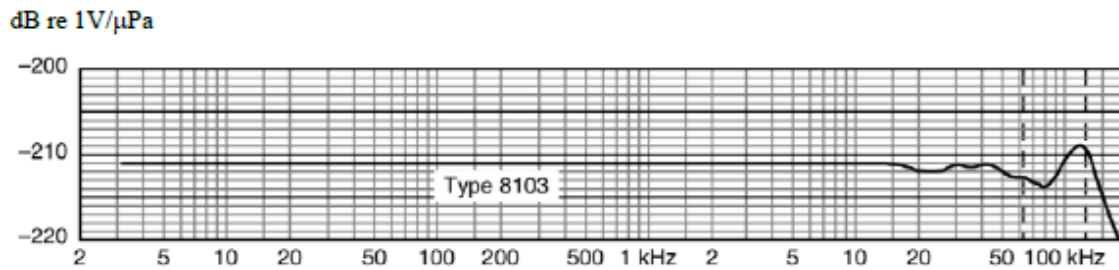
Directional Response:
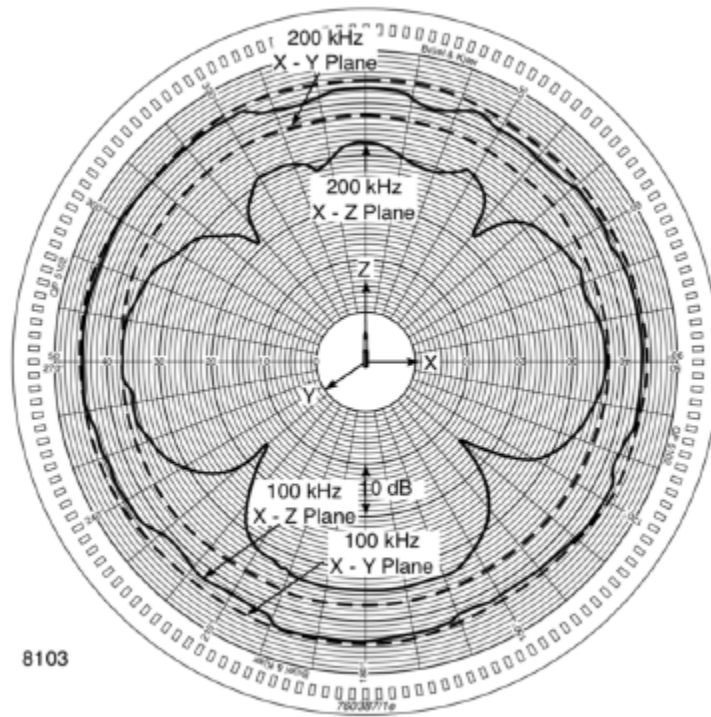
APPENDIX B. UNDERWATER AMPLIFIER SPECIFICATIONS

This appendix provides the settings used for amplification during the course of this research.

SR560 PRE-AMPLIFIER FOR HYDROPHONE

Model: Stanford Research Systems SR560 Low-Noise Amplifier

Gain: Variable in 1, 2, or 5 x 10^2, x 10^3, or x 10^4 values. $2\text{x}10^3$ setting was used.

Low-Pass Frequency: 1000 Hz

Low-Pass Roll Off: 6 dB/oct

High-Pass Frequency: 100 Hz

High-Pass Roll Off: 6 dB/oct

Coupling: AC

Low Noise Gain: Enabled

HP467A FOR UW30 UNDERWATER SOUND PROJECTOR

Model: HP467A Power Amplifier

Gain: 10X

THIS PAGE INTENTIONALLY LEFT BLANK

APPENDIX C. UW30 UNDERWATER LOUDSPEAKER

This appendix provides the manufacturer specifications and dimensions for the UW30 underwater loudspeaker used in this research [33].

Specifications:

Versions Available:
UW30 .... 50 feet of cable (15.24 m)
System Type: .... Underwater loudspeaker system
Frequency Response: .... 100-10,000 Hz
Power Handling, (500-5,000 Hz pink noise): .... 30 watts
Impedance: ....Nominal: 8 ohms
Dispersion: ....Omnidirectional underwater

Operating Depth: ....Up to 3.0 m (10.0 ft) below surface of water
Recommended Installation Depth: .... 1.2 m (4.0 ft)
Finish: ....Pool blue
Dimensions,
   Overall Diameter: ....182.6 mm (7.19 in.)
   Depth: ....66.3 mm (2.61 in.)
Shipping Weight: ....1.8 kg (4.0 lb)

Dimensions:
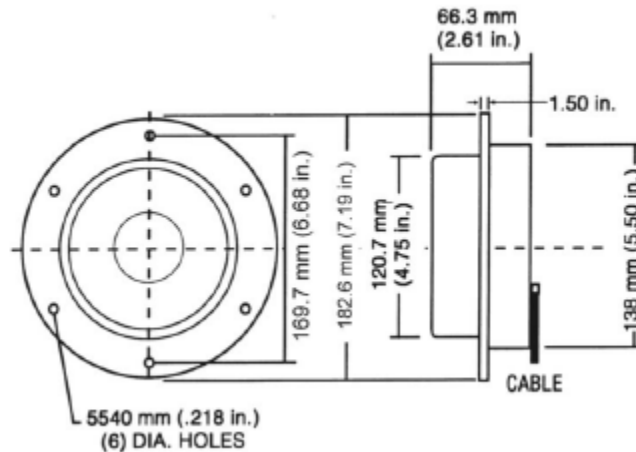
THIS PAGE INTENTIONALLY LEFT BLANK

LIST OF REFERENCES

[1]   D. A. Abraham and M. Siderius, *Underwater Acoustic Signal Processing: Modeling, Detection, and Estimation.* Charm, Switzerland: Springer, 2019.

[2]   C. Westerfield, "Towed array sonar: Uses and design challenges," AMETEK ECP, March 6, 2019. [Online]. Available: https://www.ametek-ecp.com/resources/blog/2019/march/towed-array-sonar-uses-and-design-challenges.

[3]   D. C. Kopp, "Identification underwater with towed array sonar," in *Pacific Maritime Conference,* 2010. [Online]. Available: https://www.ausairpower.net/SP/DT-TAS-Dec-2009.pdf.

[4]   S. G. Lemon, "Towed-array history, 1917–2003," *IEEE Journal of Oceanic Engineering,* vol. 29, no. 2, pp. 365–373, Jul. 2004. [Online]. doi: https://doi.org/10.1109/JOE.2004.829791.

[5]   R. Miles, D. Robert and R. Hoy, "Mechanically coupled ears for directional hearing in the parasitoid fly Ormia ochracea," *The Journal of the Acoustical Society of America,* vol. 98, no. 6, pp. 3059–3070, Jun. 1995. [Online]. doi: https://doi.org/10.1121/1.413830.

[6]   P. Braca, K. D. Lepage, P. Willet, S. Marano and V. Matta, "Particle filtering approach to multistatic underwater sensor networks with left-right ambiguity," in *16th International Conference on Information Fusion (FUSION 2013)*, Istanbul, 2013. [Online]. Available: https://ieeexplore.ieee.org/abstract/document/6641287.

[7]   S. L. Ehrlich and P. D. Frelich. "Sonar transducer," U.S. Patent 3290646 Dec. 6, 1966. [Online]. Available: https://patents.google.com/patent/US3290646A/en.

[8]   S. L. Ehrlich, N. Serotta, and K. Kleinschmidt, "Multimode Ceramic Transducers," *The Journal of the Acoustical Society of America*, vol. 31, no. 6, pp. 854–854, Jun. 1959. [Online]. doi: https://doi.org/10.1121/1.1936213.

[9]   L. L. Beranek and T. J. Mellow, *Acoustics Sound Fields and Transducers*. Oxford: Academic Press, 2012.

[10]   F. Edalatfar *et al.*, "A Wideband, Low-Noise Accelerometer for Sonar Wave Detection," *IEEE Sensors Journal*, vol. 18, no. 2, pp. 508–516, Jan. 2018. [Online]. doi: https://doi.org/10.1109/JSEN.2017.2774705.

[11]   R. Dymond, A. Sapienza, L. Troiano, P. Guerrini, and A. Maguer, "New vector sensor design and calibration measurements," in *Proc. of the Fourth International Conf. of Underwater Acoustic Measurements: Technologies and Results*, Kos Island, Greece, 2011.

[12] T. Akal, H. E. de Bree, B. Gur, "Hydroflown based low frequency underwater acoustical receiver," in *Proc. of the Fourth Internet Conf. & Exhibition in Underwater Acoustics Measurements: Technologies and Results*, Kos Island, Greece, 2011, pp. 871-878.

[13] J. C. Shipps and K. Deng, "A miniature vector sensor for line array applications," in *Oceans 2003. Celebrating the Past ... Teaming Toward the Future (IEEE Cat. No.03CH37492)*, 2003. [Online]. doi: https://doi.org/10.1109/OCEANS.2003.178284.

[14] C. B. Leslie, J. M. Kendall, and J. L. Jones, "Hydrophone for Measuring Particle Velocity," *The Journal of the Acoustical Society of America*, vol. 28, no. 4, pp. 711–715, Jul. 1956. [Online]. doi: https://doi.org/10.1121/1.1908455.

[15] W. D. Swan, "Bio-inspired MEMS direction finding acoustic sensor for air and underwater applications," M.S. thesis, Dept. of Physics, NPS, Monterey, CA, USA, 2016.

[16] G. E. Da Re, "MEMS underwater direction finding acoustic sensor," M.S. thesis, Dept. of Physics, NPS, Monterey, CA, USA, 2018.

[17] A. Espinoza, "Packaging and characterization of bio-inspired underwater MEMS directional sound sensor," M.S. thesis, Dept. of Physics, NPS, Monterey, CA, USA, unpublished, 2019.

[18] Clearco Products Co., Inc., *NP-PSF-2cSt Silicone Heat Transfer Fluid*, NP-PSF-2cSt, 2020. [Online]. Available: https://www.clearcoproducts.com/pdf/heat-transfer-fluids/NP-PSF-2cSt-Silicone-Heat-Transfer-Fluid-Freeze.pdf.

[19] Clearco Products Co., Inc., *NP-PSF-1cSt (octamethyltrisiloxane)*, NP-PSF-1cSt, 2020. [Online]. Available: https://www.clearcoproducts.com/pdf/volatile/NP-PSF-1cSt.pdf.

[20] M. M. Saleem and A. Somá, "Design optimization of RF-MEMS switch considering thermally induced residual stress and process uncertainties," *Microelectronics Reliability,* vol. 55, no. 11, pp. 2284–2298, Nov. 2015. [Online]. doi: https://doi.org/10.1016/j.microrel.2015.07.026.

[21] R. H. Downey and G. Karunasiri, "Reduced residual stress curvature and branched comb fingers increase sensitivity of MEMS acoustic sensor," *Journal of Microelectromechanical Systems,* vol. 23, no. 2, pp. 417–423, Apr. 2014. [Online]. doi: https://doi.org/10.1109/JMEMS.2013.2279017.

[22] COMSOL, Inc., Burlington, MA. 2018. COMSOL Multiphysics, ver. 5.4. [Online]. Available: https://www.comsol.com/.

[23] T. Klose, H. Conrad, T. Sandner and H. Schenk, "Fluidmechanical damping analysis of resonant micromirrors with out-of-plane comb drive," in *COMSOL Conference*, Hannover, 2008. [Online]. Available: https://www.comsol.com/paper/download/37065/Klose.pdf

[24] I. J. Tashev, *Sound Capture and Processing: Practical Approaches*. Chichester, West Sussex, UK: John Wiley and Sons, 2009.

[25] Norland Products Incorporated, *Norland Optical Adhesive 68*, 0057-CP, 2020. [Online]. Available: https://www.norlandprod.com/literature/68tds.pdf.

[26] B. Gureck, "Resolving bearing ambiguity with a single bio-inspired direction finding MEMS acoustic sensor," M.S. thesis, Dept. of Physics, NPS, Monterey, CA, USA, unpublished, 2020.

[27] PCB Piezotronics, *PCB model 378A21*, 378A21_C, 2016. [Online]. Available: https://www.pcb.com/contentstore/docs/PCB_Corporate/Vibration/Products/Specsheets/378A21_C.pdf.

[28] PCB Piezotronics, *PCB model 482C16*, 482C16_F, 2016. [Online]. Available: https://www.pcb.com/contentstore/docs/PCB_Corporate/Electronics/Products/Specsheets/482C16_F.pdf.

[29] Keysight Technologies, *E3620A and E3630A non-programmable DC power supplies*, 5967-9727, 2018. [Online]. Available: https://www.keysight.com/us/en/assets/7018-06784/data-sheets/5968-9727.pdf.

[30] ANSI/ASA S1.20-2012, "Procedures for calibration of underwater electroacoustic transducers," *The Journal of the Acoustical Society of America,* vol. 138, no. 3, pp. 1822–1822, Sep. 2015. [Online]. doi: https://doi.org/10.1121/1.4933782.

[31] Bruel & Kjaer, *Hydrophone types 8103, 8104, 8105 and 8106*, BP0317-22, 2019. [Online]. Available: https://www.bksv.com/-/media/literature/Product-Data/bp0317.ashx.

[32] Stanford Research Systems, *SR560 low-noise pre-amplifier datasheet*, SR560, 2020. [Online]. Available: https://www.thinksrs.com/downloads/pdfs/catalog/SR560c.pdf.

[33] Electro-Voice, *UW30 EDS*, 38109-847, 2010. [Online]. Available: https://www.electrovoice.com/binary/UW30%20EDS.pdf.

[34] *HP 467A Power Amplifier/Supply Operating & Service Manual*, Hewlett-Packard, Loveland, CO, USA, 1965. [Online]. Available: https://www.pearl-hifi.com/06_Lit_Archive/15_Mfrs_Publications/20_HP_Agilent/HP_467A_Op_Serv.pdf.

[35]	Loctite, "*Loctite PL marine sealant technical data sheet*, 2020627, 2015. [Online]. Available: https://dm.henkel-dam.com/is/content/henkel/TDS-2020627-US-Loctite-PL-Marine-Fast-Cure-Adhesive-Sealant-Carded-Tube-Plastic-Cartridge-3-oz-10-1-fl-oz-2015-05-20pdf.

INITIAL DISTRIBUTION LIST

1.   Defense Technical Information Center
        Ft. Belvoir, Virginia

2.   Dudley Knox Library
        Naval Postgraduate School
        Monterey, California